

176

Measurement of the D^{*+} Branching Fractions

by

Oliver Bardon

B.A., Physics
University of Virginia, 1988

Submitted to the Department of Physics
in partial fulfillment of the requirements for the degree of

Doctor of Philosophy

at the

MASSACHUSETTS INSTITUTE OF TECHNOLOGY

June 1995

© Massachusetts Institute of Technology, 1995. All Rights Reserved.

Author

Department of Physics
May 26, 1995

Certified by 

 Richard K. Yamamoto, PhD
Professor of Physics
Thesis Supervisor

Accepted by

George Koster, PhD
Chairman, Graduate Committee

MASSACHUSETTS INSTITUTE OF TECHNOLOGY

JUN 26 1995

Science

Measurement of the D^{*+} Branching Fractions

by

Oliver Bardon

Submitted to the Department of Physics on May 26, 1995

in partial fulfillment of the requirements

for the degree of Doctor of Philosophy

A significant discrepancy exists between recent measurements of the D^{*+} branching fractions and the pre-existing world average values. A measurement of these branching fractions has been made using some 27 pb^{-1} of e^+e^- collisions at 4.03 GeV center of mass energy collected by the Beijing Spectrometer experiment at the Beijing Electron Positron Collider. At this energy, $D\bar{D}^*$ pair production events are distinguishable from $D^*\bar{D}^*$ and $D\bar{D}$ events using the distinct momentum spectra of the D mesons produced in each type of event. The numbers of D mesons reconstructed in the $D^0 \rightarrow K^-\pi^+$ and $D^+ \rightarrow K^-\pi^+\pi^+$ modes in $D\bar{D}^*$ events have been counted, and from these numbers the D^{*+} branching fractions have been extracted. The results are consistent with the current world average.

Thesis Supervisor: Richard K. Yamamoto

Title: Professor of Physics

Acknowledgements

I thank first of all my advisor, Richard Yamamoto, for his boundless patience and perseverance in helping me to learn how to be a physicist. His dedication to teaching, his concern for his students, and his enthusiasm for his profession have been instrumental in making my graduate education enjoyable and successful.

I am grateful to all my collaborators on the BES experiment and the staff of IHEP for their tremendous efforts. I give special thanks to Bill Dunwoodie, Eric Soderstrom, Walter Toki, Bruce Lowery, and Mike Kelsey for their considerate and enthusiastic help and advice. I also thank my collaborators on the SLD experiment, from whom I learned very much.

I have been lucky to be associated with the outstanding people in the LQS group. Ray Cowan and Mike Fero have always been willing to put time and thought into my many questions, and I thank them particularly for their considerable help in getting started when I first arrived at SLAC. It has been a pleasure to work together with my fellow students Jim Quigley and Eric Torrence, who have done much to make graduate student life not only bearable, but often a pretty good time.

Finally, I am most grateful to my family. I thank my parents, Marcel and Renate, for their constant support and encouragement in everything that I have done. I thank my wife, Chris, for her faith in me, her help and support in every aspect of my life, and her love and companionship. Together they have made everything I have accomplished possible. I dedicate this thesis to them.

Table of Contents

1	Motivation.....	11
1.1	Introduction.....	11
1.2	Previous Measurements	13
1.3	Importance of the D^{*+} Branching Fraction Measurement	14
1.4	Object of This Experiment.....	15
2	Experimental Apparatus.....	16
2.1	The Beijing Electron Positron Collider.....	16
2.2	The Beijing Spectrometer	17
3	Data Accumulation	23
3.1	Electron - Positron Collisions at 4.03 GeV Center of Mass Energy.....	23
3.2	Triggering	23
3.3	Experimental Runs.....	24
4	Monte Carlo Simulation.....	26
4.1	General Approach	26
4.2	D^* and D Physics Simulation.....	26
4.3	Determination of Individual Track Efficiencies	27
5	Analysis Method	30
5.1	D^* Physics at 4.03 GeV	30
5.2	D^{*+} Branching Fraction Measurement Methods	31
5.3	Discussion of Analysis Methods.....	35
6	Measurement.....	36
6.1	Event Selection and Identification.....	36
6.2	Measurement of N_{D^0}	38
6.3	Measurement of N_{D^+}	45
6.4	Extraction of the D^{*+} Branching Fractions.....	49
6.5	Summary	50
Appendix A Error Analysis.....		52
Appendix B Angular Distributions		56

List of Figures

Figure 1.1: D^* decay diagrams.	12
Figure 2.1: Schematic of the BEPC.	16
Figure 2.2: Transverse view of the BES detector.	18
Figure 2.3: Axial view of the BES detector.	19
Figure 2.4: Truncated dE/dx pulse height vs. momentum.	21
Figure 2.5: TOF beta vs. momentum.	22
Figure 4.1: Detection efficiencies for individual charged tracks.	29
Figure 5.1: D momentum spectra.	30
Figure 6.1: Invariant mass distributions for $D^0 \rightarrow K^- \pi^+$ decays (Monte Carlo) reconstructed with correct and reversed mass assignments.	40
Figure 6.2: Background to $D^0 \rightarrow K^- \pi^+$ signal from other D decays in $D\bar{D}^*$ events (Monte Carlo)	42
Figure 6.3: Gaussian-plus-polynomial fits to D^0 mass distributions.	43
Figure 6.4: Gaussian-plus-polynomial fits to D^+ mass distributions	47
Figure 6.5: Sideband fits to D^+ mass distributions.	48

List of Tables

Table 1.1: Masses and lifetimes of some states involved in this analysis.	11
Table 1.2: Previous D^{*+} branching fractions and world averages.	13
Table 5.1: D momenta from production at $E_{CM} = 4.03$ GeV	30
Table 6.1: Results of measurements of N_{D^0}	44
Table 6.2: Comparison between expected and fit D^0 background scale factors.	44
Table 6.3: Results of measurements of N_{D^+}	49
Table 6.4: Results for the D^{*+} branching fractions.	50

Chapter 1

Motivation

1.1 Introduction

The D^* meson consists of a charm quark and an up or down antiquark.¹ It has a spin of one, indicating that the two quark spins are aligned. Some parameters of the D^* mesons (and of several other states involved in this analysis) are given in Table 1.1 [1]. The D^{*+} meson decays via three modes: to $D^+\gamma$, $D^+\pi^0$, and $D^0\pi^+$. The D^{*0} meson decays only to $D^0\gamma$ and $D^0\pi^0$; the decay $D^{*0} \rightarrow D^+\pi^-$ does not occur since the D^{*0} mass is less than the sum of the D^+ and π^- masses. These decays are illustrated in Fig. 1.1. All these decays are strong or electromagnetic processes and the D^* lifetime is therefore very short. Several significant D decay modes are well measured, providing means of identifying the parent D^* mesons.

Name	Quark Content	Mass (MeV)	c * Mean Lifetime	Spin / Parity Assignment (J^P)
D^{*0}	$\bar{c}u$	2006.7 ± 0.5	? (very short)	1^-
D^{*+}	$\bar{c}d$	2010.0 ± 0.5	? (very short)	1^-
D^0	$\bar{c}u$	1864.6 ± 0.5	124 μm	0^-
D^+	$\bar{c}d$	1869.4 ± 0.4	317 μm	0^-
π^+	$u\bar{d}$	139.5690 ± 0.0004	7.8 m	0^-
π^0	$\frac{1}{\sqrt{2}}(u\bar{u} - d\bar{d})$	134.9764 ± 0.0006	25 nm	0^-
K^-	$s\bar{u}$	493.68 ± 0.02	3.7 m	0^-

Table 1.1: Masses and lifetimes of some states involved in this analysis.

1. Reference to a specific particle or decay also implies the charge conjugate particle or decay throughout this text, unless specified otherwise.

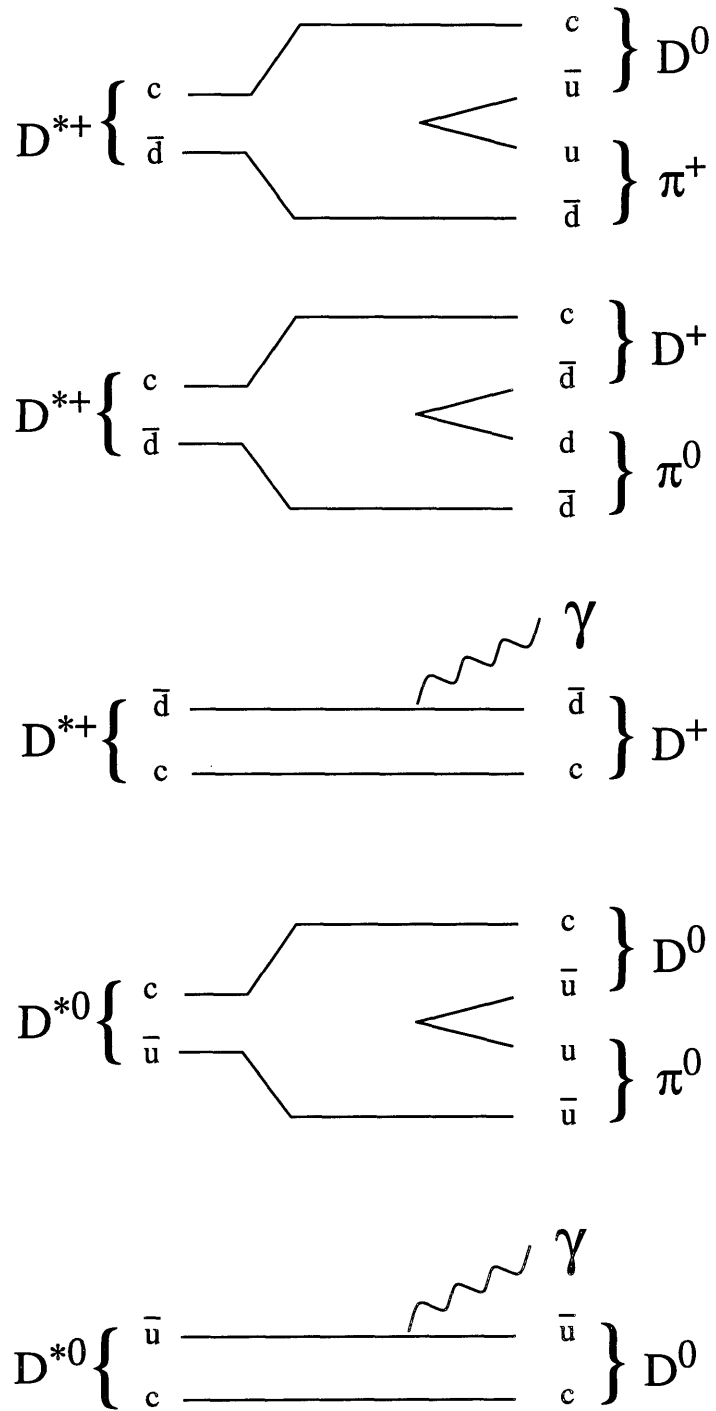


Figure 1.1: D^* decay diagrams.

1.2 Previous Measurements

There is a significant discrepancy between the two most recent D^{*+} branching fraction measurements and the world average existing prior to them (Table 1.2). Before 1992, the

Branching Fractions (%)	$B(D^{*+} \rightarrow D^0\pi^+)$	$B(D^{*+} \rightarrow D^+\pi^0)$	$B(D^{*+} \rightarrow D^+\gamma)$
Mark III (1988)	$57 \pm 4 \pm 4$	$26 \pm 2 \pm 2$	$17 \pm 5 \pm 5$
PDG (1992)	55 ± 4	27.2 ± 2.5	18 ± 4
CLEO II (1992)	$68.1 \pm 1.0 \pm 1.3$	$30.8 \pm 0.4 \pm 0.8$	$1.1 \pm 1.4 \pm 1.6$
PDG (1994)	68.1 ± 1.3	30.8 ± 0.8	$1.1^{+1.4}_{-0.7}$
ARGUS (1994)	$68.5 \pm 3.4 \pm 3.2$	$31.5 \pm 2.7 \pm 3.0$	$0.0 \pm 2.9 \pm 1.6$

Table 1.2: Previous D^{*+} branching fractions and world averages (in chronological order).

most precise measurement was made in 1988 by the Mark III experiment [2] using the SPEAR e^+e^- storage ring at the Stanford Linear Accelerator Center. $D\bar{D}^*$ and $D^*\bar{D}$ (and $D\bar{D}$) pairs were produced at a center of mass energy (E_{CM}) of 4.14 GeV. The directly produced and secondary D mesons were reconstructed, and a fit was made to the recoil mass squared¹ spectrum. The fit was compared with a Monte Carlo model to extract the corresponding D^{*+} branching fractions. This result dominated the world average (as determined by the Particle Data Group (PDG) [5]) until 1992.

Another measurement was made in 1992 by the CLEO II experiment [3] using the CESR e^+e^- storage ring at Cornell. D^* mesons were produced in the decays of B mesons produced near the Υ resonance (around $E_{CM} = 10$ GeV). The D^{*+} mesons decaying to $D^+\gamma$ and $D^+\pi^0$ were fully reconstructed. The ratio of the $D^{*+} \rightarrow D^+\pi^0$ and $D^{*+} \rightarrow D^0\pi^+$ branching fractions was constrained using a phase space and isospin con-

1. The recoil mass squared u is defined as $u = (E_{CM} - E_D)^2 - P_D^2$, where E_D and P_D are the D energy and momentum.

ervation relationship.¹ The CLEO II results were much more precise than and significantly different from the Mark III values. The latest PDG values [1] are identical to those found by CLEO II. The ARGUS experiment [4] was very similar to the CLEO II experiment, and it obtained very similar results.

1.3 Importance of the D^{*+} Branching Fraction Measurement

The D^* meson is an example of a heavy quark (c) - light quark ($\bar{u}\bar{d}$) system. This type of system is believed to be well described by existing models (in particular, the constituent quark model [6, 7] and the cloudy bag model [8]), which have been very successful in modeling other heavy quark-light quark experimental observations. The heavy quark is considered to be approximately the center of mass of the system and is treated non-relativistically, while the light quark moves relativistically around it. Particularly accurate predictions are expected for the ratio of the D^{*0} and D^{*+} radiative decay rates. The predicted ratio is consistent with the two most recent measurements [9]. The Mark III measurement implies either a failure of these models or some non-standard extension. The radiative decay rates are functions of the quark magnetic moments, and the larger Mark III value indicates an anomalously large charm quark magnetic moment. One possible explanation for such an anomaly is that the charm quark may be a composite object [8].

Accurate D^{*+} branching fractions are also required for physics studies not directly related to the D^* mesons. In particular, the D^{*-} is a major decay product of B mesons ($\mathcal{B}(B \rightarrow D^{*-}X) = 23\%$ [1]), and the branching fractions will be important for upcoming high-statistic B physics studies.

1. The same relationship is used in this analysis (Eq. 5.1)

1.4 Object of This Experiment

This experiment made an independent measurement of the D^{*+} branching fractions, using a completely different technique from those described above. The goal of the measurement was to provide a check of the previous results, and to attempt to resolve the discrepancy between them.

Chapter 2

Experimental Apparatus

2.1 The Beijing Electron Positron Collider

The Beijing Electron Positron Collider (BEPC) [10] is located at the Institute of High Energy Physics (IHEP) in Beijing. A schematic of the collider is shown in Fig. 2.1. The main linac accelerates electrons and positrons to energies between 1.1 and 1.4 GeV. They are further accelerated to steady beam energies of between 1.5 and 2.2 GeV in the storage ring. The ring operates with one bunch of particles per beam. The collision frequency is 1.25 MHz. The peak luminosity at $E_{CM} = 4.03$ GeV is $8 \times 10^{30} \text{ cm}^{-2} \text{ s}^{-2}$, although typical operating luminosities were around 1 to $2 \times 10^{30} \text{ cm}^{-2} \text{ s}^{-2}$ for this experiment. Filling the storage ring typically took about 30 minutes, and the collider could operate efficiently for one to two hours before requiring a new fill. The storage ring has two interaction regions: the BES detector occupied one, and the other was vacant during this experiment.

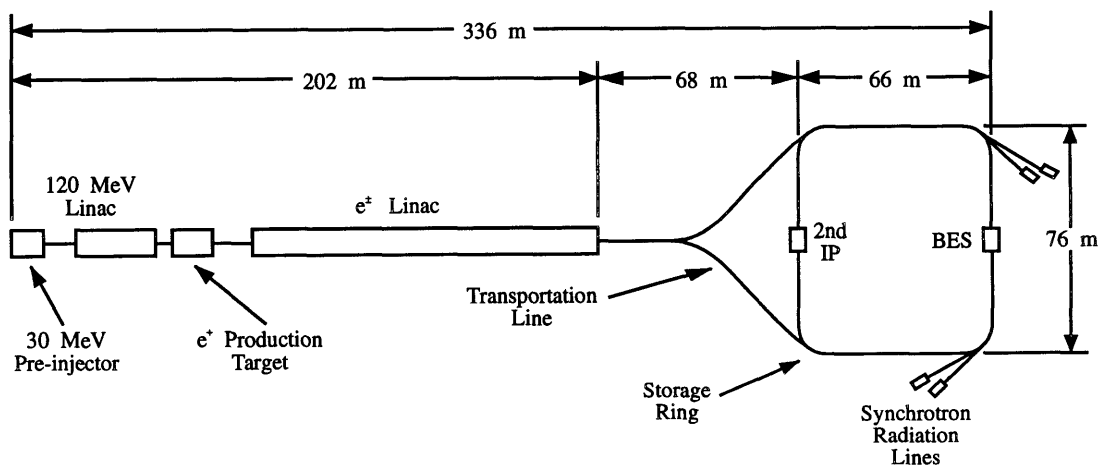


Figure 2.1: Schematic of the BEPC.

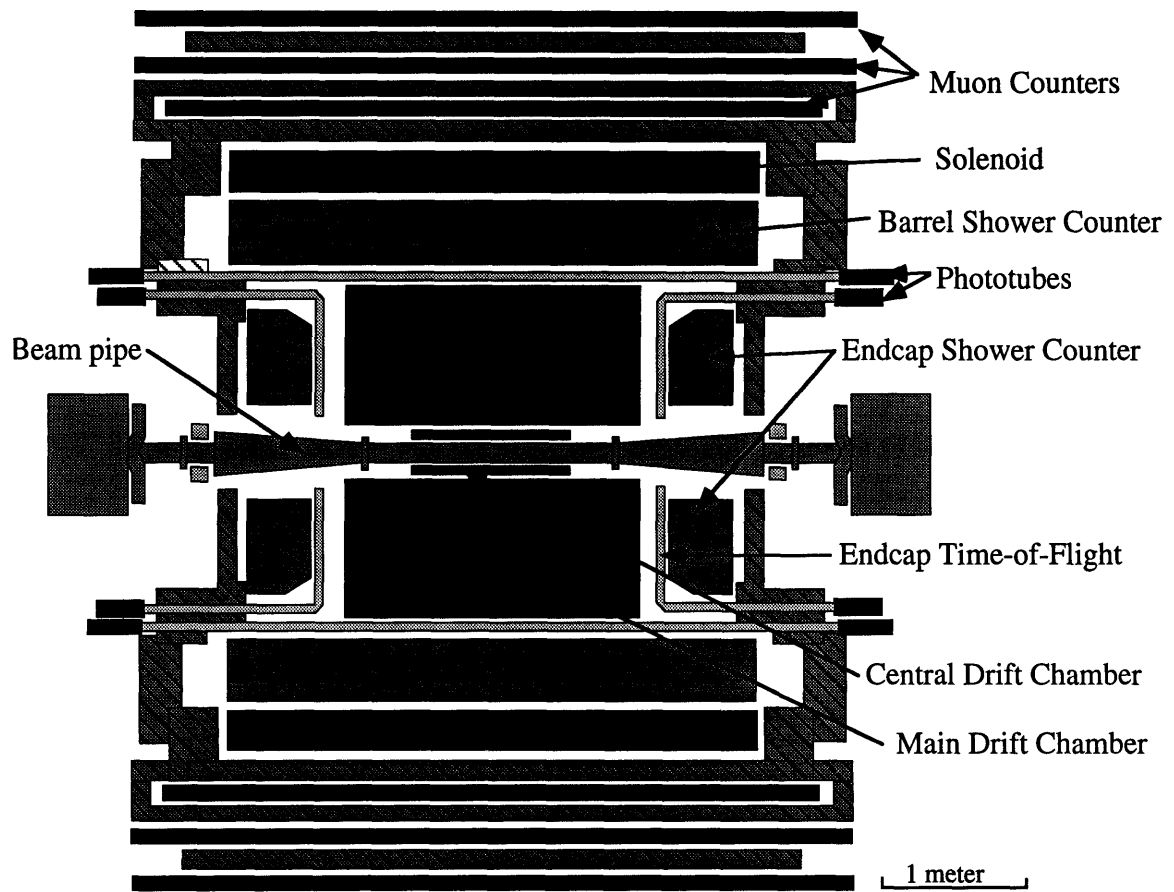
2.2 The Beijing Spectrometer

The Beijing Spectrometer (BES) [10] (Figs. 2.2 and 2.3) is a multi-component device designed to measure charged and neutral particles over nearly the entire solid angle around the interaction point. The barrel part of the detector, from innermost component outward, consists of a four-layer central drift chamber (CDC), a 40-layer main drift chamber (MDC), a ring of 48 time-of flight (TOF) counters, and a 24-layer lead-gas sampling calorimeter (shower counter), all of which are arranged cylindrically symmetrically around the aluminum storage ring beampipe. A 0.4 Tesla solenoid encloses the barrel components. An iron yoke outside the solenoid provides flux return for the magnetic field and contains three double-layer sets of proportional tubes used for muon detection. The endcap TOF and shower counters cover the regions near the beampipe. Luminosity monitors immediately next to the beampipe detect small-angle bhabhas.

All of the barrel components were used in the trigger (section 3.2); however, only the MDC and barrel TOF were used directly in this analysis.

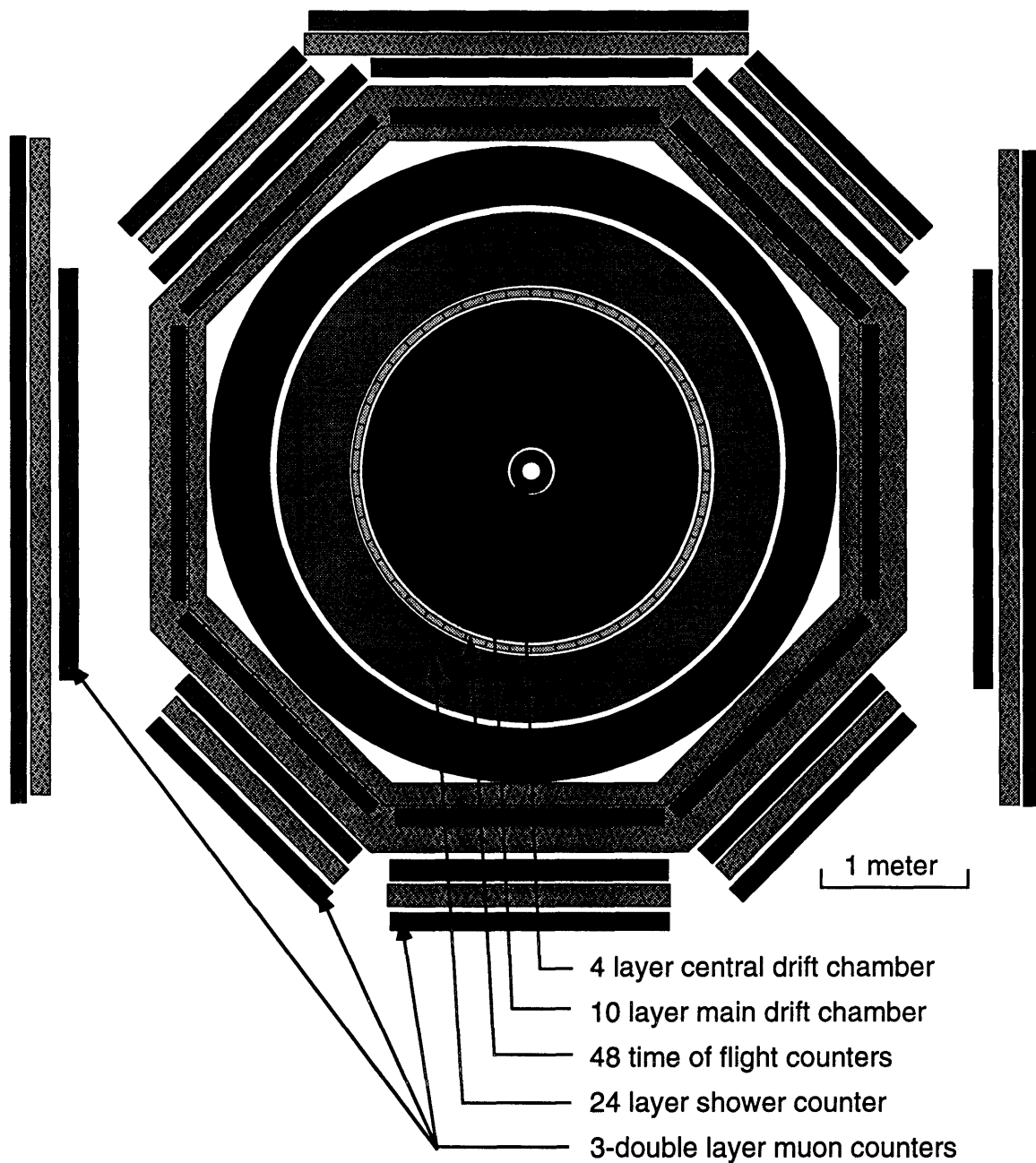
2.2.1 The Main Drift Chamber

The MDC provides tracking, momentum, and particle identification information. Charged particles ionize the gas in the chamber, and the freed electrons drift in a uniform electric field toward the sense wires. The primary electrons avalanche in a high field region near the sense wire, and the time and size of this pulse are recorded. From the drift times, the positions of the primary ionizations can be found and the particle track can be reconstructed. From the curvature of the track in the magnetic field, the particle momentum can be calculated. The 40 concentric layers of sense wires are grouped into ten superlayers. The odd-numbered superlayers are stereo layers, with angles of two to five degrees with respect to the beam direction to provide z-coordinate information. The four sense



BES Detector

Figure 2.2: Transverse view of the BES detector.



BES Detector

Figure 2.3: Axial view of the BES detector.

wires in each superlayer cell are staggered from the radial midplane of the cell to provide local left-right ambiguity resolution. The spatial resolution for this experiment was between 200 and 250 μm , and the momentum resolution was $\sigma_p/p = 0.21 \times \sqrt{1 + p^2}$ (p = momentum in GeV).

The pulse heights measure a particle's rate of ionization. The mean rate of ionization, or dE/dx (energy loss through ionization per distance traveled), is related to the particle velocity and is independent of its mass. This relation is described by the Bethe-Bloch formula [11]. The actual ionization energy losses are Landau fluctuations about a mean. The mean is estimated by ignoring the highest 30% of the pulse height measurements for a given track and averaging the rest. Given the particle momentum and the dE/dx measurement of the velocity, the mass can be deduced. For this experiment, the MDC provided 2σ separation between pions and kaons with momenta up to 550 MeV.

2.2.2 The Time-of-Flight Counter

The TOF counter measures the time at which a particle passes through the counter with respect to the beam crossing time. The counter is made up of 48 scintillator strips, each 15 cm. wide and 2 m. long. Light guides at both ends of each strip bring the photons to photomultiplier tubes. The beam crossing time is measured by electrodes near the beampipe which sense the pulses induced by the passing bunches. The bunches are each some 5 cm. long and they overlap for about 170 ps. This uncertainty in the interaction time contributes directly to the uncertainty in the TOF measurement. The TOF resolution for hadrons was between 400 and 500 ps for this experiment. This range includes degradation due to scintillator aging. Given the particle path and momentum from the MDC measurements, the velocity and mass can be deduced. For this experiment, the TOF provided 2σ separation between pions and kaons with momenta up to 650 MeV.

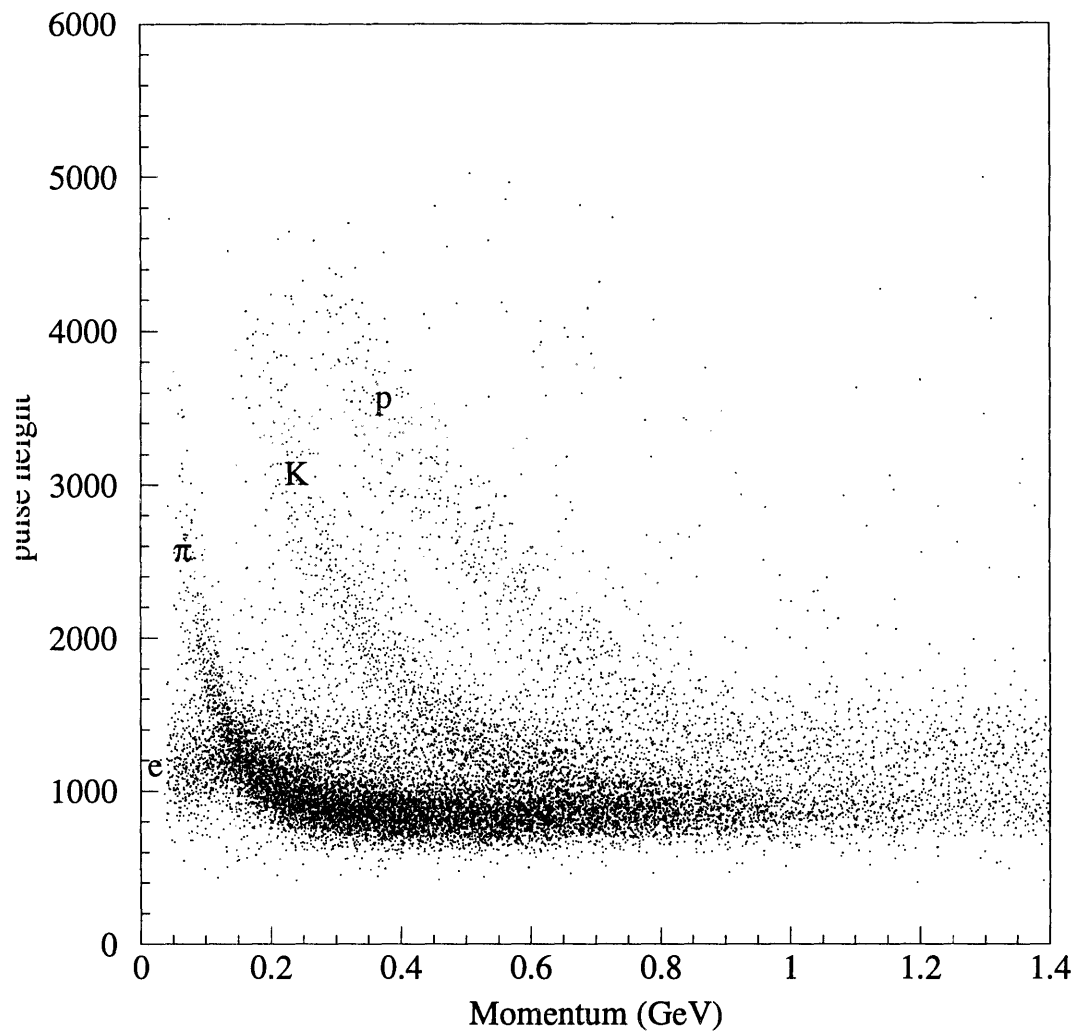


Figure 2.4: Truncated dE/dx pulse height vs. momentum. Separate bands are visible corresponding to electrons and positrons (e), pions (π), kaons (K), and protons and anti-protons (p).

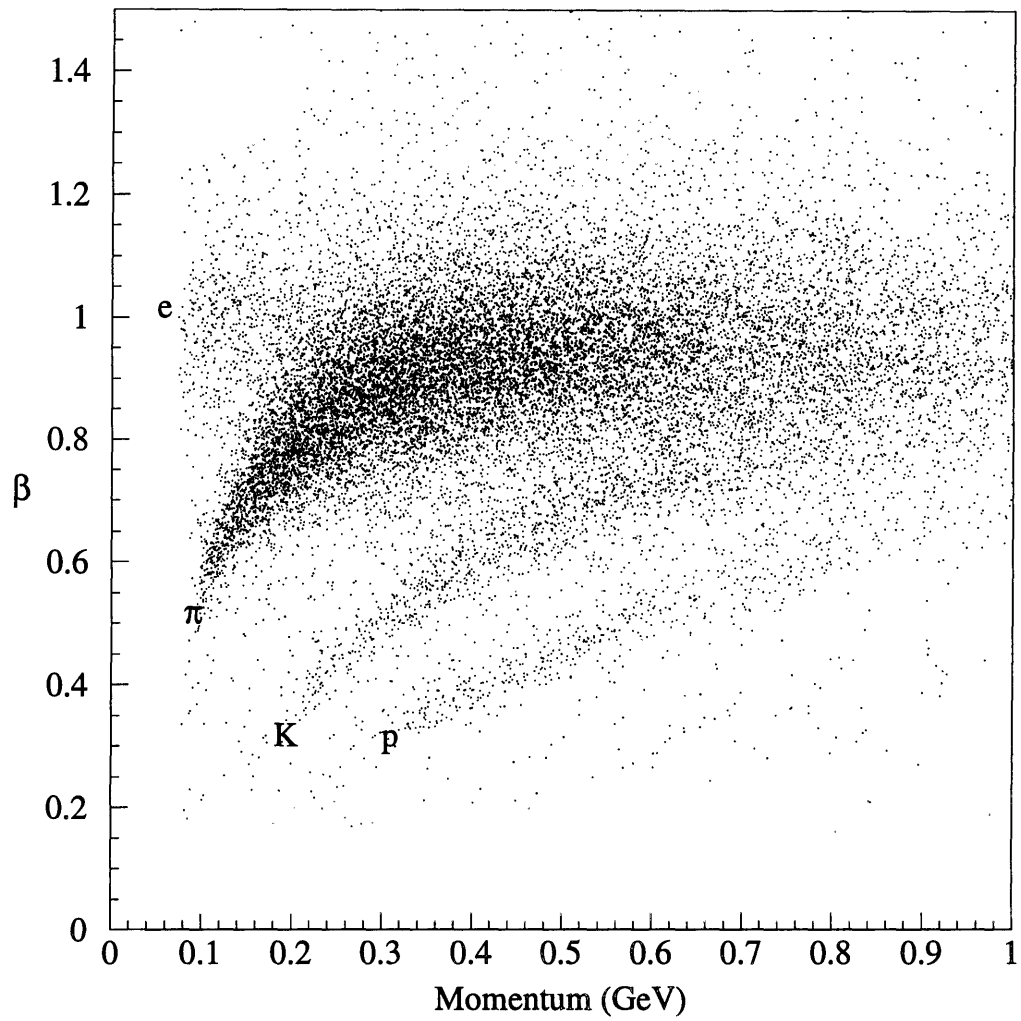


Figure 2.5: TOF beta vs. momentum. Separate bands are visible corresponding to electrons and positrons (e), pions (π), kaons (K), and protons and anti-protons (p).

Chapter 3

Data Accumulation

3.1 Electron - Positron Collisions at 4.03 GeV Center of Mass Energy

The data used in this analysis were accumulated at the BEPC at a center of mass energy of 4.03 GeV. This energy was chosen to maximize the production of D_s mesons via the reaction $e^+e^- \rightarrow D_s \bar{D}_s$. This choice of energy was based on the Eichten model [12], which predicts that D_s pair production will peak at this energy, and on data from several experiments [13,14] which indicated a peak in total hadronic cross section at this energy. As it turns out, much of the peak observed by Crystal Ball is due to $D\bar{D}^*$ and $D^*\bar{D}$ pair production.

3.2 Triggering

With a bunch collision rate of 1.25 MHz, only a small fraction of the e^+e^- interactions which occurred could be measured by the detector, and only a small fraction of those measured could be written to tape. An on-line trigger consisting of output from several detector components was used to decide quickly which events were likely to be interesting and should be recorded. The trigger conditions represented a compromise between different goals:

- to make the total amount of data written to tape manageable
- to minimize the rejection of interesting events (i.e., to keep the efficiency high)
- to minimize the detector operating time used recording uninteresting events

Charm events were the object of the all analyses performed with this data set; in addition, wide-angle bhabhas and $\mu^+\mu^-$ pairs were useful for luminosity measurement and detector calibration. The general characteristics of these event types were high momentum tracks

in the drift chamber, large energy deposition in the shower counter, and hits in the muon detection system. The trigger was a logical OR of the following criteria:

1. At least two drift chamber tracks each with associated barrel TOF hits.
2. At least 1 GeV total energy deposition in the barrel shower counter.
3. At least one hit in the innermost muon detector layer.

The typical trigger rate was between five and 10 Hz.

3.3 Experimental Runs

The data used here were accumulated during three separate running periods between the Spring of 1992 and the Spring of 1994. In addition to minor equipment and operations problems expected in such a complex system, there was one major problem during each running period.

In the 1992 run, 3.3 pb^{-1} of data were accumulated. It was discovered about two thirds of the way through this run that the drift chamber time-to-amplitude converter (TAC) threshold was set too high, resulting in reduced efficiencies both for triggering and for reconstructing tracks in recorded events. This threshold was reduced for the final third of the 1992 run. Because of this change, the 1992 run was divided into two parts for the purpose of determining detector efficiency from Monte Carlo.

During the 1993 run, an intermittent timing shift in the drift chamber pulse height readout electronics resulted in the loss of dE/dx information for some 36% of the run. Since pulse height was also involved in track reconstruction¹, the events with no dE/dx information were not used in physics analyses. Fortunately these events were easily iden-

1. Drift chamber electron drift time was measured by a TDC (time-to-digital converter) which recorded the time at which a pulse from a sense wire crossed a discriminator threshold. For a given actual drift time, a larger pulse with a faster rise time would cross the threshold earlier than a smaller pulse. This effect was accounted for in reconstruction using a factor which was a function of pulse height.

tified. The total integrated luminosity for the 1993 run was 7.3 pb^{-1} , of which 4.7 pb^{-1} with good dE/dx information are used in this analysis.

The 1994 run was by far the most productive, with 14.7 pb^{-1} accumulated. However, during this run there were small systematic shifts in beam energy away from the nominal 2.015 GeV . It was not possible to reconstruct these shifts precisely, and as a result there was a relatively large systematic uncertainty ($\sim \pm 2 \text{ MeV}$) in the E_{CM} value for this period. This uncertainty was very significant for analyses involving $D^* \bar{D}^*$ events, as will be described later. However, it had little effect on $D \bar{D}^*$ analyses.

Chapter 4

Monte Carlo Simulation

4.1 General Approach

Monte Carlo simulation was used to study the expected signal and background characteristics and to determine the detection efficiencies. The simulation consisted of two parts: one which modeled the production and decay of charmed particles, and one which modeled the detector response. The charm physics simulation was based on existing models (e.g., decay angular distributions) and measurements (e.g., decay branching fractions). The detector simulation was similarly based both on models (e.g., multiple scattering of particles in the various detector media) and on actual measurements made with the detector. These calibration measurements were made with well-understood, high-statistic processes (e.g., J/Ψ and Ψ' decays).

Detection efficiencies were used to relate the number of observed events to the number that were actually produced. Two types of efficiencies were determined:

- Individual track efficiency, which accounted for detector response and for the efficiency of the reconstruction algorithm. This efficiency was applied to each reconstructed track.
- Global efficiency, which accounted for physics effects, such as the angular and momentum distributions of the produced particles, and for the efficiency of the analysis algorithm. This efficiency was applied to the reconstructed sample as a whole.

4.2 D^* and D Physics Simulation

The simulation process began with the decay of a 4.03 GeV virtual photon into a pair of charmed particles. $D\bar{D}^*$, $D^*\bar{D}$, and $D\bar{D}$ events were generated separately. The D^* mesons

were decayed at the same time, and care was taken to model the joint angular distributions of the charm pair production and D^* decays (described in detail in Appendix B). The D mesons were then decayed via the various intermediate D decay states into long lived states (leptons, pions, kaons, photons). These particles and the secondary pions and photons from the D^* decays were propagated through the detector simulation.

The current world averages used for the D^* decay mode branching fractions were identical to those measured by CLEO II. Simulations showed that the reconstruction efficiencies for D mesons were nearly identical for each of the D^* decay modes. In addition, simulations using different sets of D^* branching fractions showed no appreciable difference in the reconstructed D mass distributions. These results indicated that no bias was introduced with a specific choice of D^* branching fractions.

A $D\bar{D}^*$ sample was generated in which both particles were allowed to decay via all possible modes according to the world average measured branching fractions. This sample was used to examine backgrounds due to the D decay modes which were not reconstructed. This sample was also useful for developing and testing the analysis which was used on the real data. $D^*\bar{D}^*$ and $D\bar{D}$ samples with both particles decaying to all modes were also produced to check for backgrounds to the $D\bar{D}^*$ signal.

The global detection efficiency for each reconstruction mode was extracted using different $D\bar{D}^*$ samples. In these samples, one D meson was forced to decay only via the mode to be reconstructed, while the other D meson could decay via all modes. The analysis algorithms were applied to these samples, and the global detection efficiencies were given by the ratios of the numbers of reconstructed D mesons to the numbers generated.

4.3 Determination of Individual Track Efficiencies

The detector simulation was used to determine the detection and reconstruction efficiency

for individual tracks as a function of particle type, momentum, and direction. Pions and kaons were generated with random momenta and propagated through the detector. High track multiplicity in an event could affect efficiency by confusing the track reconstruction; the particles were therefore generated with the same multiplicity distribution as seen in the real data. The number reconstructed was compared with the number thrown as a function of momentum, polar angle, and azimuthal angle. The efficiencies were found to be independent of azimuthal angle. The momentum and polar angle efficiency distributions (Fig. 4.1) were used to construct individual efficiencies for the real data tracks.

Some elements of the detector changed during the experiment. Variable factors included adjustments, aging, and failures of components and readout electronics (for example, those described in section 3.3). These variations were accounted for in the simulation with different sets of calibration constants. The constants were based on known changes in the detector (e.g., dead readout channels) and on brief calibration physics runs (e.g., Ψ' production) interspersed throughout the 4.03 GeV runs. Four sets of constants were produced, one each for the 1993 and 1994 runs, and two for the 1992 run, as described in section 3.3. Separate sets individual track efficiencies were determined using each set of calibration constants. In addition, the Monte Carlo samples described in section 4.2 were generated using each set of constants in proportion to the amount of data taken under each set of conditions.

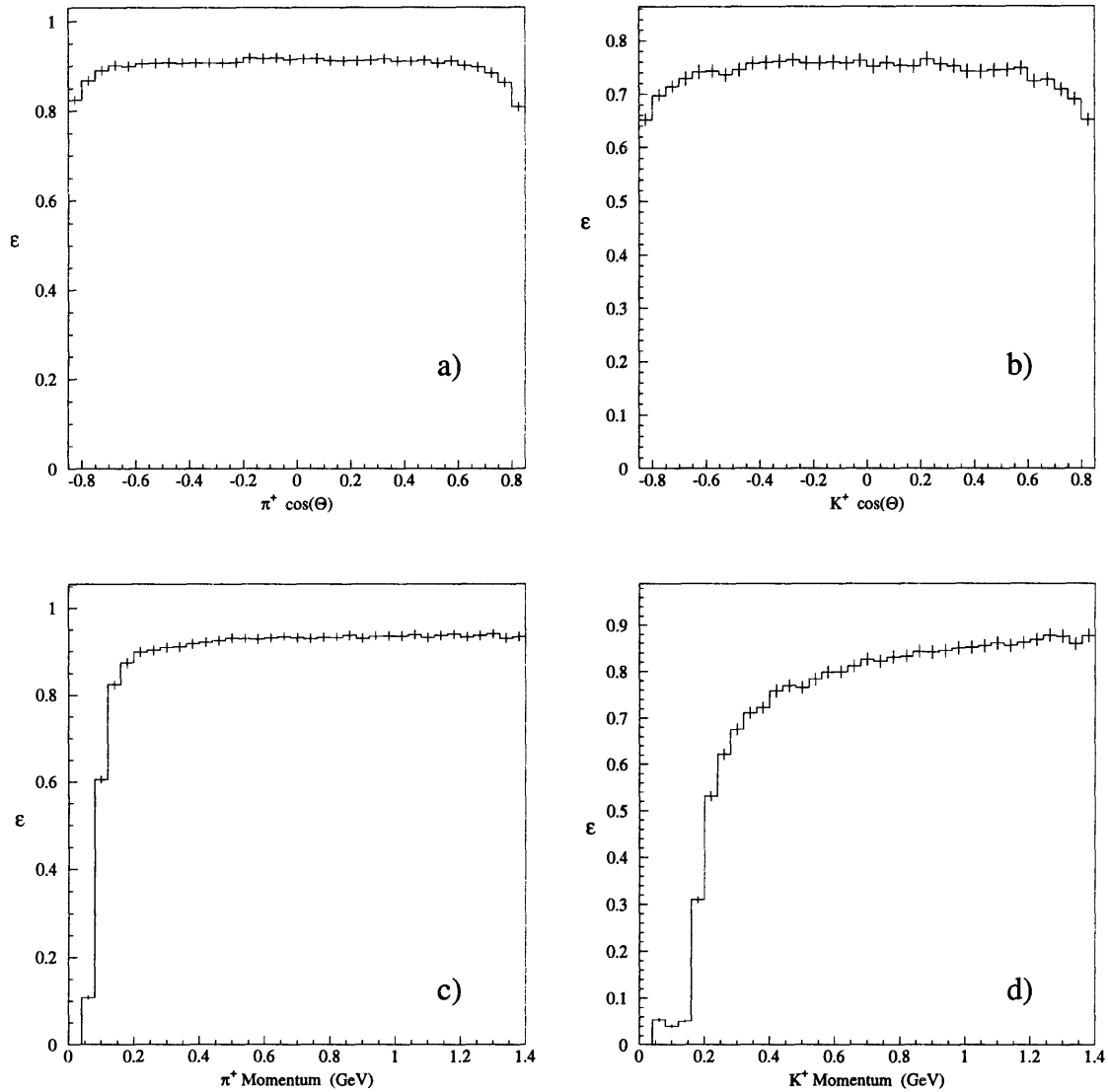


Figure 4.1: Detection efficiencies for individual charged tracks, determined from Monte Carlo: a) pions as a function of $\cos\theta$; b) kaons as a function of $\cos\theta$; c) pions as a function of momentum; d) kaons as a function of momentum.

Chapter 5

Analysis Method

5.1 D^* Physics at 4.03 GeV

At 4.03 GeV center of mass energy, D^* and D mesons are produced only in the reactions $e^+e^- \rightarrow D\bar{D}^*$, $e^+e^- \rightarrow D^*\bar{D}$, and $e^+e^- \rightarrow D\bar{D}$. At this energy, the momentum spectra of D mesons, both primary and secondary (from $D^* \rightarrow D\gamma$ and $D^* \rightarrow D\pi$), from each of these three reactions are distinct (Table 5.1). This fact allows the selection of independent pure $D\bar{D}^*$ and $D^*\bar{D}$ event samples, based on the momentum of reconstructed D candidates.

Production Mode	Momentum Range
$D^*\bar{D}$	$.004 \text{ GeV} < P_D < .308 \text{ GeV}$
$D\bar{D}^*$	$.368 \text{ GeV} < P_D < .664 \text{ GeV}$
$D\bar{D}$	$P_{D^0} = .752 \text{ GeV}, P_{D^+} = .764 \text{ GeV}$

Table 5.1: D momenta from production at $E_{CM} = 4.03 \text{ GeV}$

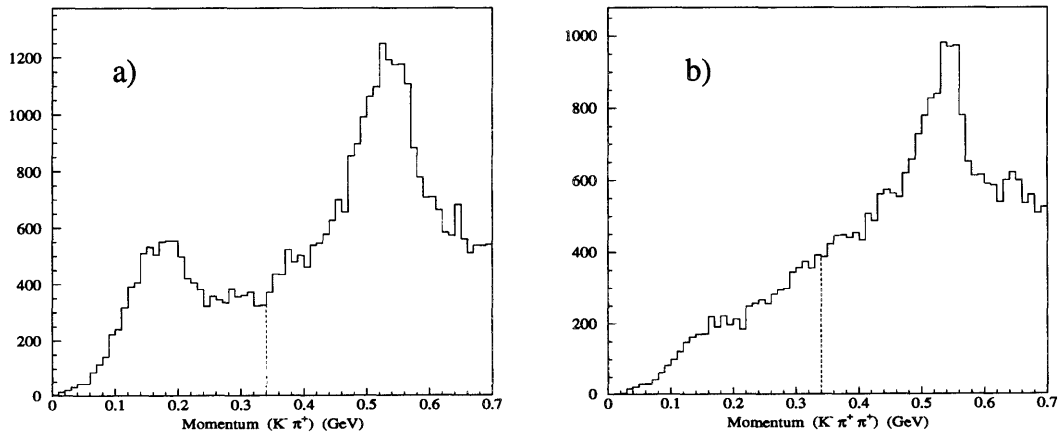


Figure 5.1: D momentum spectra. The D mesons are reconstructed in the a) $D^0 \rightarrow K \pi^+$ and b) $D^+ \rightarrow K \pi^+ \pi^+$ modes. The dashed lines indicate the midpoints between the $D^*\bar{D}$ and $D\bar{D}^*$ spectra. The D^+ signal in the $D^*\bar{D}$ range is small because the $D^{*+}D^{*-}$ cross section is very small at $E_{CM} = 4.03 \text{ GeV}$.

Both the D^* and D mesons produced at this energy mostly decay within a millimeter of their production vertices. D candidates must therefore be identified by their longer-lived decay products which pass through the detector. In this analysis, D mesons decaying via the $D^0 \rightarrow K^- \pi^+$ and $D^+ \rightarrow K^- \pi^+ \pi^+$ channels are reconstructed.¹ These kaons and pions have sufficiently long lifetimes and high momenta to be efficiently identified and measured. D candidate reconstruction is discussed in detail in Chapter 6.

It would also be useful to reconstruct fully D^* candidates, by identifying both the secondary D meson and its accompanying pion or photon. However, at 4.03 GeV the momenta of these pions and photons are very low ($P_\pi < 84\text{MeV}$, $P_\gamma < 181\text{MeV}$) and it was not possible to reconstruct these particles with any efficiency.

5.2 D^{*+} Branching Fraction Measurement Methods

The D^{*+} branching fractions can be related to the observed number of D mesons. First, note that every D^{*0} meson decays to a D^0 meson (and an accompanying pion or photon). The fraction of D^{*+} decays that produce a D^0 meson is equal to the $D^{*+} \rightarrow D^0 \pi^+$ branching fraction ($B(D^{*+} \rightarrow D^0 \pi^+) \equiv B_{\pi^+}$).² Because the three D^{*+} branching fractions are assumed to add up to one (unitarity constraint), the fraction of D^{*+} decays that produce a D^+ meson is given by $1 - B_{\pi^+}$. B_{π^+} can then be related to the observed numbers of D mesons in each type of event ($D\bar{D}^*$ and $D^* \bar{D}$) and can be extracted from a measurement of these numbers. These relationships are described in detail below.

1. Doubly Cabibbo suppressed $D^0 \rightarrow K^- \pi^+$ decays are also reconstructed. This branching fraction is added to the $D^0 \rightarrow K^- \pi^+$ fraction, since no distinction is made between D^0 and \bar{D}^0 decays in this analysis.

2. As a reminder, invariance under charge conjugation is assumed throughout this analysis, and reference to a specific particle or decay also implies the charge conjugate particle or decay. For example, $B(D^{*+} \rightarrow D^0 \pi^+) = B(D^{*-} \rightarrow \bar{D}^0 \pi^-) \equiv B_{\pi^+}$.

With a measurement of B_{π^+} and the unitarity constraint, one more constraint is needed to extract the other two D^{*+} branching fractions. It is obtained by assuming that the two $D^{*+} \rightarrow D\pi$ decay rates are identical except for isospin conservation and phase space factors:

$$\frac{B(D^{*+} \rightarrow D^+\pi^0)}{B(D^{*+} \rightarrow D^0\pi^+)} = \frac{1}{2} \cdot \frac{P_{D^+}^3}{P_{D^0}^3} \quad (5.1)$$

where the factor of 1/2 is due to isospin conservation, and P_D is the D momentum in the D^* rest frame.

5.2.1 D^{*+} Branching Fractions from $D\bar{D}^*$ Events

Consider first the $D\bar{D}^*$ event sample. The D^0 and D^+ production cross sections¹ σ_{D^0} ($= \sigma_{D^0}$) and σ_{D^+} ($= \sigma_{D^+}$) for $D\bar{D}^*$ events can be expressed as a function of B_{π^+} and the $D\bar{D}^*$ cross sections $\sigma_{D^0D^{*0}}$ ($= \sigma_{D^0D^{*0}}$) and $\sigma_{D^+D^{*-}}$ ($= \sigma_{D^+D^{*-}}$):

$$\begin{aligned} \sigma_{D^0} &= \sigma_{D^0D^{*0}} && \text{from the primary } D^0 \\ &+ \sigma_{D^0D^{*0}} && \text{from } D^{*0} \rightarrow D^0X \\ &+ B_{\pi^+} \cdot \sigma_{D^+D^{*+}} && \text{from } D^{*+} \rightarrow D^0\pi^+ \\ &= 2 \cdot \sigma_{D^0D^{*0}} + B_{\pi^+} \cdot \sigma_{D^+D^{*-}} && (5.2) \end{aligned}$$

$$\begin{aligned} \sigma_{D^+} &= \sigma_{D^+D^{*-}} && \text{from the primary } D^+ \\ &+ \left(1 - B_{\pi^+}\right) \cdot \sigma_{D^+D^{*+}} && \text{from } D^{*+} \rightarrow D^+X \\ &= \left(2 - B_{\pi^+}\right) \cdot \sigma_{D^+D^{*-}} && (5.3) \end{aligned}$$

Assuming that charged and neutral $D\bar{D}^*$ pairs are produced at equal rates except for phase space factors,

1. The cross section is defined as the number produced per unit luminosity.

$$r = \frac{\sigma_{D^0 D^{*0}}}{\sigma_{D^- D^{*+}}} = \frac{P_{D^{*0}}^3}{P_{D^{*+}}^3} \quad (5.4)$$

where $P_{D^{*0}}$ and $P_{D^{*+}}$ are the D^* momenta.

The ratio of the D^+ and D^0 cross sections can be expressed as

$$R = \frac{\sigma_{D^+}}{\sigma_{D^0}} = \frac{N_{D^+}^{obs} \cdot B(D^0) \cdot \epsilon_{D^0} \cdot L}{N_{D^0}^{obs} \cdot B(D^+) \cdot \epsilon_{D^+} \cdot L} = \frac{N_{D^+} \cdot B(D^0)}{N_{D^0} \cdot B(D^+)} \quad (5.5)$$

where $N_{D^0}^{obs}$ and $N_{D^+}^{obs}$ are the number of reconstructed D mesons; $B(D^0)$ is the D^0 decay branching fraction $B(D^0 \rightarrow K^- \pi^+)$; $B(D^+)$ is the D^+ decay branching fraction $B(D^+ \rightarrow K^- \pi^+ \pi^+)$; ϵ_{D^0} and ϵ_{D^+} are the D reconstruction global efficiencies; L is the integrated luminosity; and $N_D = N_D^{obs} / \epsilon_D$. Combining equations 5.2 - 5.5,

$$B_{\pi^+} = \frac{2(1-rR)}{1+R} \quad (5.6)$$

B_{π^+} can then be related to the two other D^{*+} decay mode branching fractions using the unitarity constraint and the relationship between the $D^{*+} \rightarrow D^+ \pi$ fractions (Eq. 5.1).

5.2.2 D^{*+} Branching Fractions from $D^* \bar{D}^*$ Events

An analogous measurement of the D^{*+} branching fractions can be made using the independent $D^* \bar{D}^*$ event sample. In this case, the D^0 and D^+ production cross sections $\sigma_{D^0}^*$ ($= \sigma_{D^0}^*$) and $\sigma_{D^+}^*$ ($= \sigma_{D^-}^*$) for $D^* \bar{D}^*$ events can be expressed as a function of B_{π^+} and the $D^* \bar{D}^*$ cross sections $\sigma_{D^0 \bar{D}^{*0}}$ and $\sigma_{D^{*+} \bar{D}^{*-}}$:

$$\sigma_{D^0}^* = 2(\sigma_{D^0 \bar{D}^{*0}} + B_{\pi^+} \sigma_{D^{*+} \bar{D}^{*-}}) \quad (5.7)$$

$$\sigma_{D^+}^* = 2(1 - B_{\pi^+}) \sigma_{D^{*+} \bar{D}^{*-}} \quad (5.8)$$

Assuming that charged and neutral $D^* \bar{D}^*$ pairs are produced at equal rates except for phase space factors,

$$r^* = \frac{\sigma_{D^{*0}D^{*0}}}{\sigma_{D^{*+}D^{*-}}} = \frac{P_{D^{*0}}^3}{P_{D^{*+}}^3} \quad (5.9)$$

The ratio of the D cross sections can be expressed as:

$$R^* = \frac{\sigma_{D^+}^*}{\sigma_{D^0}^*} = \frac{N_{D^+}^{*obs} \cdot B(D^0) \cdot \epsilon_{D^0}^* \cdot L}{N_{D^0}^{*obs} \cdot B(D^+) \cdot \epsilon_{D^+}^* \cdot L} \quad (5.10)$$

where $N_{D^+}^{*obs}$ and $N_{D^0}^{*obs}$ are the number of reconstructed D mesons, and $\epsilon_{D^0}^*$ and $\epsilon_{D^+}^*$ are the D reconstruction global efficiencies. Combining equations 5.7 - 5.10,

$$B_{\pi^+} = \frac{1 - r^* R^*}{1 + R^*} \quad (5.11)$$

B_{π^+} again can be related to the other D^{*+} branching fractions using the unitarity and isospin/phase space constraints.

5.2.3 D^{*+} Branching Fractions Combining $D^* \bar{D}^*$ and $D \bar{D}^*$ Events

A measurement of the D^{*+} branching fractions can also be made combining the observed number of D mesons in both $D \bar{D}^*$ and $D^* \bar{D}^*$ events as follows:

$$\frac{N_{D^+}^{*obs}}{N_{D^+}^{obs}} = \frac{\sigma_{D^+}^* \cdot B(D^+) \cdot \epsilon_{D^+}^* \cdot L}{\sigma_{D^+} \cdot B(D^+) \cdot \epsilon_{D^+} \cdot L} = r_+ \cdot \frac{2(1 - B_{\pi^+}) \epsilon_{D^+}^*}{(2 - B_{\pi^+}) \epsilon_{D^+}} \quad (5.12)$$

$$\frac{N_{D^0}^{*obs}}{N_{D^0}^{obs}} = \frac{\sigma_{D^0}^* \cdot B(D^0) \cdot \epsilon_{D^0}^* \cdot L}{\sigma_{D^0} \cdot B(D^0) \cdot \epsilon_{D^0} \cdot L} = r_+ \cdot \frac{2(r^* + B_{\pi^+}) \epsilon_{D^0}^*}{(2r + B_{\pi^+}) \epsilon_{D^0}} \quad (5.13)$$

where

$$r_+ = \frac{\sigma_{D^{*+}D^{*-}}}{\sigma_{D^+D^+}} \quad (5.14)$$

Combining equations 5.12 and 5.13,

$$B_{\pi^+} = \frac{(1 - 2r - 2\alpha + \alpha r^*) + [(1 - 2r - 2\alpha + \alpha r^*)^2 - 8(\alpha - 1)(r - \alpha r^*)]^{1/2}}{2(1 - \alpha)} \quad (5.15)$$

where

$$\alpha = \frac{N_{D^+}^{*obs} \epsilon_{D^+} N_{D^0}^{obs} \epsilon_{D^0}^*}{N_{D^+}^{obs} \epsilon_{D^+}^* N_{D^0}^{*obs} \epsilon_{D^0}} \quad (5.16)$$

Again, the other D^{*+} branching fractions are extracted from B_{π^+} using the unitarity and isospin/phase space constraints.

5.3 Discussion of Analysis Methods

The analysis methods presented above have several advantages and disadvantages with respect to one another. The first two methods provide equivalent and statistically independent measurements of the D^{*+} branching fractions. In practice, however, the $D^*\bar{D}^*$ measurement has two significant disadvantages. First, since the available center of mass energy is very near twice the D^* masses, the $D^*\bar{D}^*$ cross sections are significantly lower than the $D\bar{D}^*$ cross sections; in particular, the $D^{*+}D^{*-}$ cross section is very small. As a result, the statistics of the $D^*\bar{D}^*$ measurement are much lower, and the statistical errors much higher. Second, again because the $D^*\bar{D}^*$ production is very near threshold, the factor r^* (Eq. 5.8), which appears in the expression for B_{π^+} (Eq. 5.10), is subject to a much larger relative error due to uncertainty in the D^* mass and the center of mass energy than the corresponding factor r which appears in Eq. 5.4.

The third method, combining both event types, has a significant advantage over the first two in that it is independent of the D decay branching fractions ($B(D^0)$, $B(D^+)$), which must be measured independently and are sources of significant systematic errors. Unfortunately, this advantage is offset by the same statistical and systematic errors which afflict the $D^*\bar{D}^*$ measurement.

The analyses involving $D^*\bar{D}^*$ events were attempted, but the $D^{*+}D^{*-}$ cross section proved to be too small for these analyses to be feasible with the available data. The $D\bar{D}^*$ measurement is presented in this thesis.

Chapter 6

Measurement

6.1 Event Selection and Identification

6.1.1 Charm Event Pre-selection

The raw data set was very large even after the application of the on-line trigger criteria and still consisted mostly of uninteresting events. A pre-selection process was therefore carried out during the data reconstruction, with only events satisfying all of the following criteria being written to tape:

- at least three tracks reconstructed in the drift chamber OR at least two photons identified in the barrel shower counter
- the average of the radial components of the impact parameters¹ of all reconstructed tracks less than 2 cm.
- the average of the z components (along the beam direction) of the impact parameters of all reconstructed tracks less than 20 cm.
- at least 1.5 GeV total scalar momentum for all charged tracks and photons in the event

This pre-selection was common to all BES charm physics analyses.

6.1.2 Track Selection Criteria for *D* Meson Reconstruction

D mesons were reconstructed from charged kaons and pions. The following criteria were applied to select kaon and pion candidate tracks:

- A radial impact parameter of less than 1 cm., and a z impact parameter of less than 15

1. The impact parameter is the distance of closest approach of a track to the nominal interaction point, as the track is extrapolated back from the drift chamber towards the interaction point.

cm. These criteria eliminated some remaining tracks that did not come from e^+e^- collisions (e.g., cosmic rays, beam-gas interactions), as well as some tracks that came from non- D meson secondary decays (e.g., $K^0 \rightarrow \pi^+\pi^-$).

- A polar angle θ (angle between the electron beam direction and the track) satisfying $|\cos\theta| < .85$. This cut required that the track pass through six layers of the drift chamber. Monte Carlo studies showed that the track reconstruction efficiency and reliability decreased rapidly with larger values of $|\cos\theta|$.
- A momentum greater than 170 MeV for each kaon candidate, and greater than 100 MeV for each pion candidate. Monte Carlo studies indicated that tracks coming from $D^+ \rightarrow K^-\pi^+\pi^+$ decays with momenta lower than these were very rarely reconstructed, resulting in a large relative error on their efficiencies.

6.1.3 Particle Identification

The TOF and dE/dx particle identification systems were used to distinguish between pions and kaons. χ^2 functions were constructed from the measured and predicted values for each particle type; for kaons:

$$\chi_{\text{TOF}}^2 (K) = \frac{[t_{\text{meas}} - t_{\text{pred}}(K)]^2}{\sigma_{\text{TOF}}^2} \quad (6.1)$$

$$\chi_{\text{dE/dx}}^2 (K) = \frac{[ph_{\text{meas}} - ph_{\text{pred}}(K)]^2}{\sigma_{\text{dE/dx}}^2} \quad (6.2)$$

and similarly for pions. These χ^2 functions were combined into a normalized likelihood ratio, or weight:

$$w_k = \frac{e^{\left(-\frac{1}{2}\right)\chi_{\text{TOF}}^2 (K)} e^{\left(-\frac{1}{2}\right)\chi_{\text{dE/dx}}^2 (K)}}{e^{\left(-\frac{1}{2}\right)\chi_{\text{TOF}}^2 (K)} e^{\left(-\frac{1}{2}\right)\chi_{\text{dE/dx}}^2 (K)} + e^{\left(-\frac{1}{2}\right)\chi_{\text{TOF}}^2 (\pi)} e^{\left(-\frac{1}{2}\right)\chi_{\text{dE/dx}}^2 (\pi)}} \quad (6.3)$$

Note that for a given track,

$$w_{\pi} = 1 - w_K \quad (6.4)$$

6.2 Measurement of N_{D^0}

6.2.1 D^0 Candidate Reconstruction

D^0 candidates were reconstructed from all combinations of pairs of oppositely charged tracks which satisfied the criteria described above (section 6.1.2). The invariant mass and momentum of each candidate were constructed using the measured momentum and the hypothesized (kaon or pion) mass of each track. Each pair of tracks was reconstructed using both hypotheses, resulting in two candidates per pair of tracks.

A joint efficiency was constructed for each candidate from the product of the individual detector track efficiencies:

$$\varepsilon_{D^0} = \varepsilon_K \cdot \varepsilon_{\pi} \quad (6.5)$$

For each pair of candidates, joint likelihoods were constructed from the products of the two individual track likelihoods, normalized by the sum of these two products:

$$w_{D^0}(\text{candidate1}) = \frac{w_K(\text{track1}) \cdot w_{\pi}(\text{track2})}{norm} \quad (6.6)$$

$$w_{D^0}(\text{candidate2}) = \frac{w_K(\text{track2}) \cdot w_{\pi}(\text{track1})}{norm} \quad (6.7)$$

where

$$norm = w_K(\text{track1}) \cdot w_{\pi}(\text{track2}) + w_K(\text{track2}) \cdot w_{\pi}(\text{track1}) \quad (6.8)$$

In some cases, two pairs of tracks shared a common track; the normalization factor was then the sum of all four individual unnormalized candidate likelihoods. More complicated track sharing could occur, but in practice, there were very rarely more than two candidate pairs in an event. With this normalized likelihood system, each pair or set of candidates sharing a track had a total likelihood (or weight) of one, and double counting was avoided.

To account for systematic effects due to particle identification, a second weighting scheme was also used. Out of each pair, the candidate with the higher likelihood was assigned a weight of one, and the other candidate was discarded. The best candidates from pairs sharing a track were each assigned a weight of 0.5. A separate global efficiency was determined using this scheme.

As a further check for systematic effects, a third scheme using no particle identification was used. Each candidate in a pair was assigned a weight of 0.5; candidates from pairs sharing a track were assigned weights of 0.25. A separate global efficiency was again determined.

Candidates were then selected by momentum to be consistent with $D\bar{D}^*$ production (see section 5.1). The invariant mass of each candidate was entered in a histogram, weighted by the candidate likelihood and the inverse of the candidate efficiency. Separate mass distributions were plotted using each weighting scheme.

6.2.2 D^0 Signal Fit

The D meson, which decays only via weak processes, has a very small intrinsic width ($\ll 1$ eV). The signal shape was therefore dominated by detector resolution. In addition, there was a significant effect due to the fact that for each correctly reconstructed D^0 , there was a partner candidate for which the kaon and pion mass assignments were reversed. Because the track momenta were large with respect to the pion - kaon mass difference, the resulting invariant mass was close to that of the correctly reconstructed partner. Monte Carlo studies showed that the incorrect invariant mass distribution peaked very near the D^0 mass (Fig. 6.1). To allow for these two signal shapes, the signal was fit with the sum of two gaussian distributions.

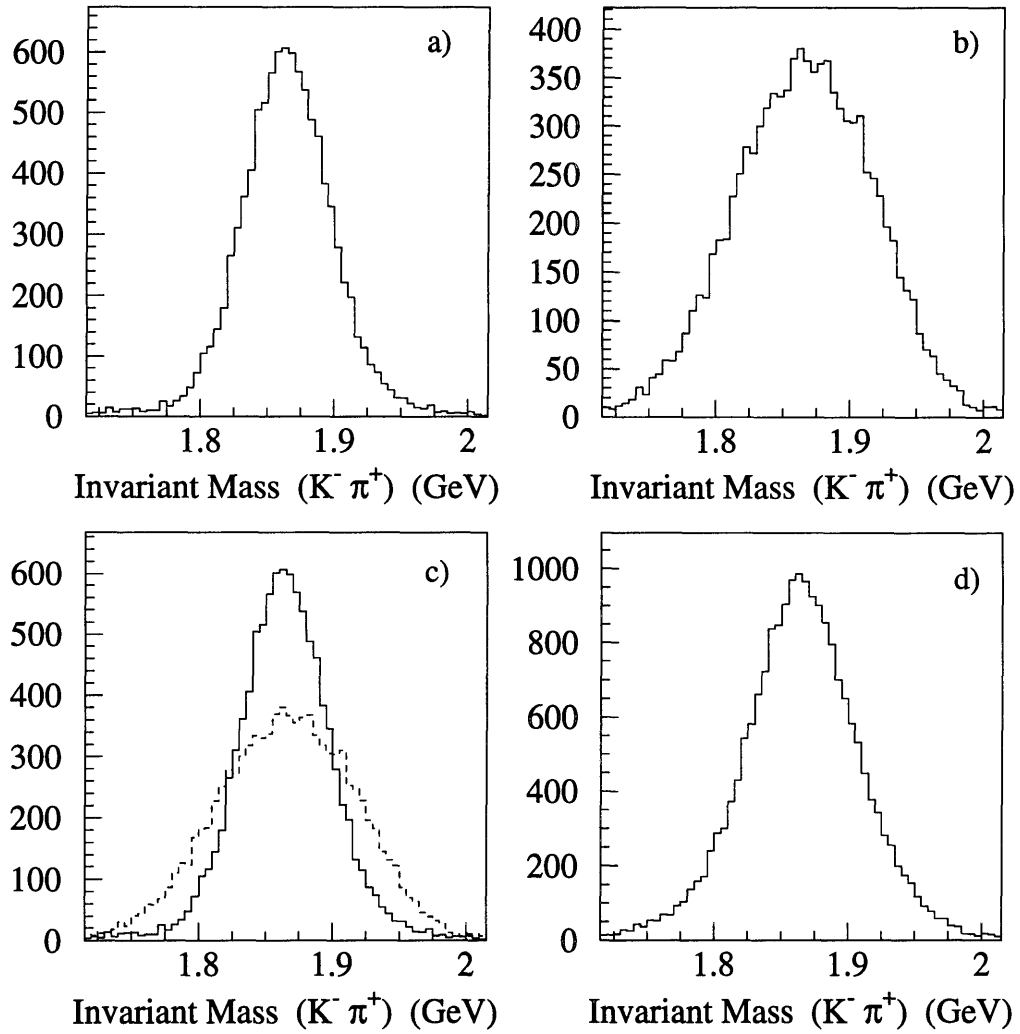


Figure 6.1: Invariant mass distributions for $D^0 \rightarrow K^- \pi^+$ decays (Monte Carlo) reconstructed with correct and reversed mass assignments: a) correct assignment; b) reversed assignment; c) overlay of a) and b); d) sum of a) and b).

The background to this signal consisted of combinations of tracks from other D decay modes and from continuum quark pair production. Monte Carlo studies indicated that because of the large kaon and pion momenta resulting from $D^0 \rightarrow K^- \pi^+$, most of the background from $D\bar{D}^*$ events originated from several specific physics processes, rather than from random track combinations (Fig. 6.2):

1. $D^0 \rightarrow K^- K^+$, in which one kaon was misidentified as a pion.
2. $D^0 \rightarrow \pi^- \pi^+$, in which one pion was misidentified as a kaon.
3. $D^0 \rightarrow K^- \pi^+ \pi^0$ and $D^+ \rightarrow K^- \pi^+ \pi^+$, in which one π^0 or π^+ was not observed.
4. $D^0 \rightarrow K^- e^+ \nu$ and $D^0 \rightarrow K^- \mu^+ \nu$, in which the e^+ or μ^+ was called a pion.

To account for this highly structured background, the total background was fit by the sum of

- a free polynomial, and
- a separate, fixed higher-order polynomial fit to the Monte Carlo $D\bar{D}^*$ decay background, multiplied by a free scale factor.

Monte Carlo $D^* \bar{D}^*$ and $D\bar{D}$ samples showed that the background due to these events was smooth in the fit region.

The fitted mass distributions using each of the three particle identification schemes are shown in Fig. 6.3.

6.2.3 D^0 Result

The signal size ($N_{D^0}^{obs}$) was extracted by counting the number of histogram entries in the signal range (1.74 - 1.99 GeV) and subtracting the integrated background fit over this range. The uncertainty in $N_{D^0}^{obs}$ was obtained from the error matrix of the fit and from the total number of candidates, as described in Appendix A. $N_{D^0}^{obs}$ was then divided by the global Monte Carlo efficiency, yielding the total number of $D^0 \rightarrow K^- \pi^+$ events in the

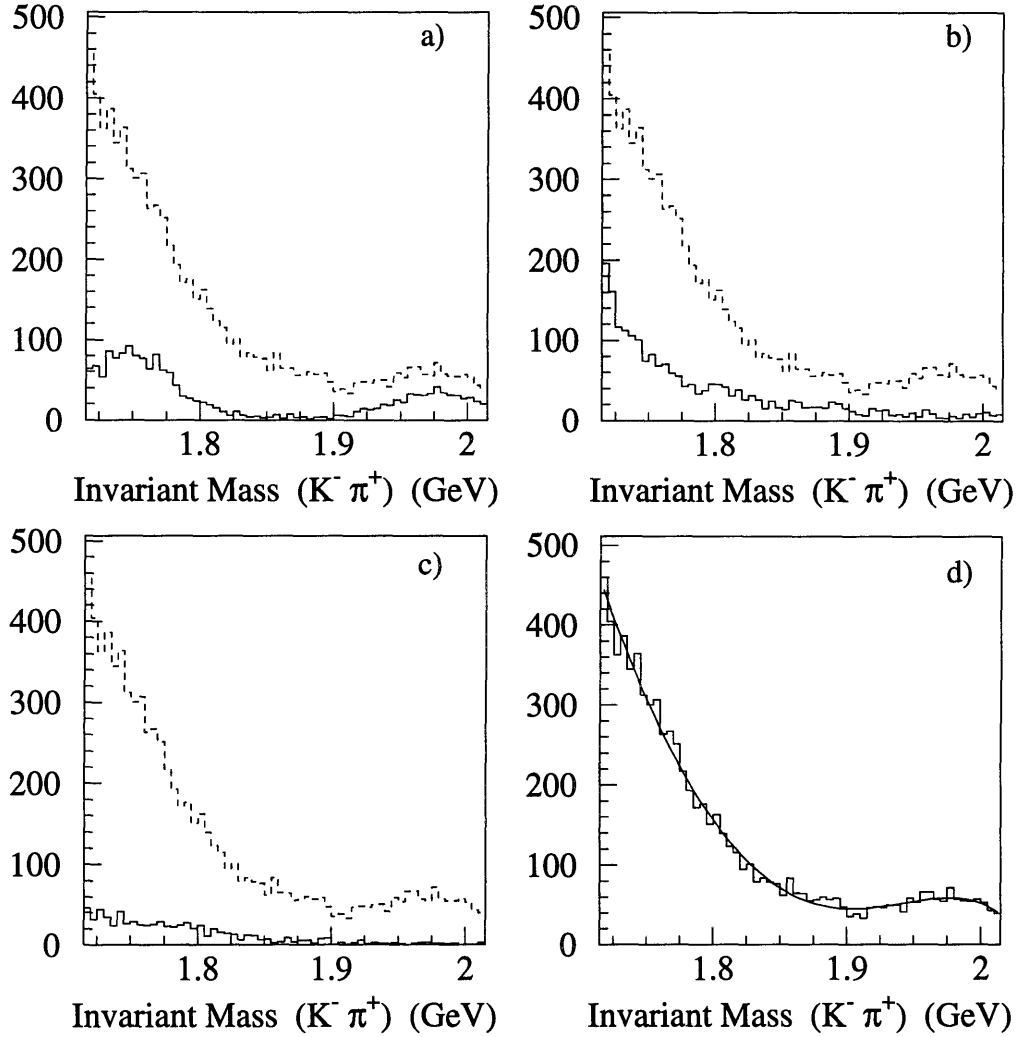


Figure 6.2: Background to $D^0 \rightarrow K^- \pi^+$ signal from other D decays in $D\bar{D}^*$ events (Monte Carlo): a) $D^0 \rightarrow K^- K^+$ (left-hand peak) and $D^0 \rightarrow \pi^- \pi^+$ decays, b) from $D^0 \rightarrow K^- \pi^+ \pi^0$ and $D^+ \rightarrow K^- \pi^+ \pi^+$ decays, and c) from $D^0 \rightarrow K^- e^+ \nu$ and $D^0 \rightarrow K^- \mu^+ \nu$ decays, each with the total $D\bar{D}^*$ background overlaid. Fig. d) shows the fit to the total background.

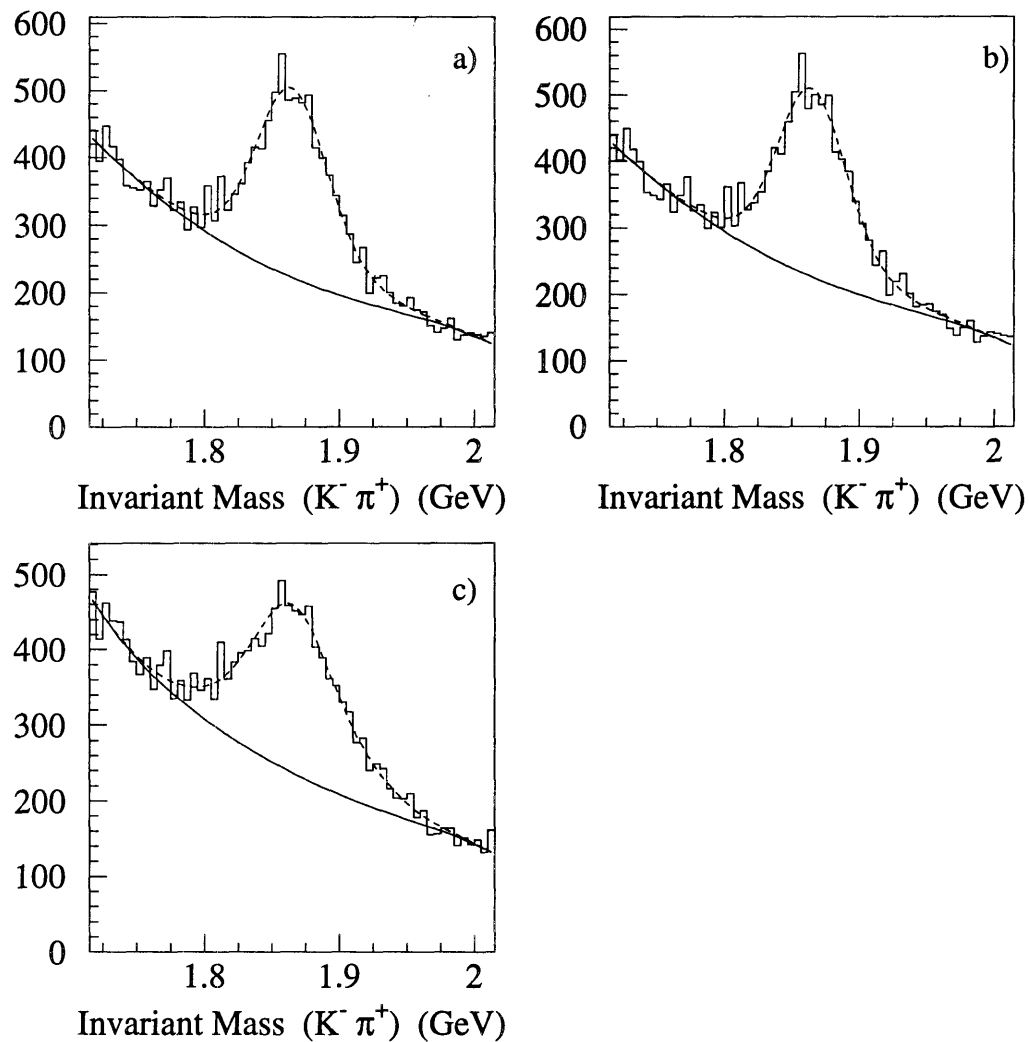


Figure 6.3: Gaussian-plus-polynomial fits to D^0 mass distributions using a) the normalized likelihood scheme, b) the best candidate scheme, and c) no particle identification.

sample (N_{D^0}). A weighted average of the results using the three particle identification schemes was taken as the final value of N_{D^0} . The systematic uncertainty on this value was set using the extrema of the individual measurements (as described in Appendix A.3). The results are shown in Table 6.1. The different particle identification methods were found to be in good agreement, and the systematic uncertainty is comparable to the standard deviation of the mean.

Particle ID Scheme	N_{D^0}
Normalized Likelihood	5468 ± 241
Best Candidate	5300 ± 255
No Particle ID	5362 ± 220
Combined	$5379 \pm 137^{+330}_{-334}$

Table 6.1: Results of measurements of N_{D^0}

The validity of the fixed $D\bar{D}^*$ background shape was checked by examining its fitted scale factor. The fixed background polynomial was obtained from a fit to a known number of $D\bar{D}^*$ Monte Carlo events (Fig. 6.2 (d)). The fitted scale factor should be equal to the ratio of the number of $D\bar{D}^*$ events in the data to the number of Monte Carlo $D\bar{D}^*$ events thrown. The total number of $D\bar{D}^*$ events in the data is equal to the measured N_{D^0} divided by the $D^0 \rightarrow K\pi^+$ branching fraction. This comparison is shown in Table 6.2. The agreement was good for all three particle identification schemes.

Particle ID Scheme	Expected Background Scale Factor	Fitted Background Scale Factor
Normalized Likelihood	0.2879 ± 0.0162	0.2928 ± 0.0390
Best Candidate	0.2791 ± 0.0166	0.2674 ± 0.0391
No Particle ID	0.2823 ± 0.0152	0.2742 ± 0.0340

Table 6.2: Comparison between expected and fitted D^0 background scale factors.

6.3 Measurement of N_{D^+}

6.3.1 D^+ Candidate Reconstruction

D^+ candidates were reconstructed from all sets of three charged tracks with a net charge of ± 1 which satisfied the criteria described in section 6.1.2. The track with charge opposite to that of the other two was assigned a kaon hypothesis, and the others were called pions (in the decay $D^+ \rightarrow K^-\pi^+\pi^+$, the kaon charge is always the opposite of the D charge). There was therefore one candidate per set of tracks.

A joint likelihood for each candidate was constructed from the product of the three individual track likelihoods. Multiple candidates in an event could share one or more tracks, and there were often multiple candidates with the same charge. The candidates in an event were separated by charge, and normalization factors were constructed for each charge type:

$$norm_+ = \sum_i (w_K(\text{track1}) \cdot w_\pi(\text{track2}) \cdot w_\pi(\text{track3}))_i \quad (6.9)$$

$$(w_{D^+})_i = \frac{(w_K(\text{track1}) \cdot w_\pi(\text{track2}) \cdot w_\pi(\text{track3}))_i}{norm_+} \quad (6.10)$$

and similarly for D^- candidates.

Two additional candidate weighting schemes were used:

1. Best candidate: the candidate likelihoods were used to pick the best candidate of each charge type. These candidates were each assigned a weight of one, and the other candidates were discarded.
2. No particle ID: no particle identification was used, and each candidate of a given charge was assigned a weight of one divided by the number of candidates with that charge.

As in the D^0 reconstruction, joint efficiencies were constructed from the products of the individual detector track efficiencies, and $D\bar{D}^*$ event candidates were selected by momentum.

6.3.2 D^+ Signal Fit

The D^+ background consisted mainly of random combinations of kaons and pions and was much larger than that of the D^0 . The signal to background ratio was low, and the extracted signal size was found to be relatively sensitive to the background fit. To account for any systematic effect due to fitting, two separate fits were made. In one, the distribution was fit with a gaussian and a polynomial background. The background uncertainty was obtained from the fit error matrix. In the other, the sidebands around the signal region (1.82 - 1.92 GeV) were fit with a polynomial, which was then interpolated under the signal region. The uncertainty in this case was estimated by varying the width of the sidebands included in the fit. The background uncertainties were considered to be uncorrelated, and the two results were combined in a weighted average. The fits were found to be in good agreement for the normalized likelihood and best candidate signals, and in reasonable agreement for the cases with no particle identification.

Monte Carlo studies showed that the backgrounds from other $D\bar{D}^*$ decays and from $D^*\bar{D}^*$ and $D\bar{D}$ events were smooth in the fit region.

The fitted mass distributions using each of the three particle identification schemes are shown in Fig. 6.4 and 6.5

6.3.3 D^+ Result

The total number of $D^+ \rightarrow K\pi^+\pi^+$ events in the sample (N_{D^+}) was extracted as in the D^0 case; the results are shown in Table 6.3. The results using each of the three particle identification schemes were found to be in reasonable agreement with one another. A

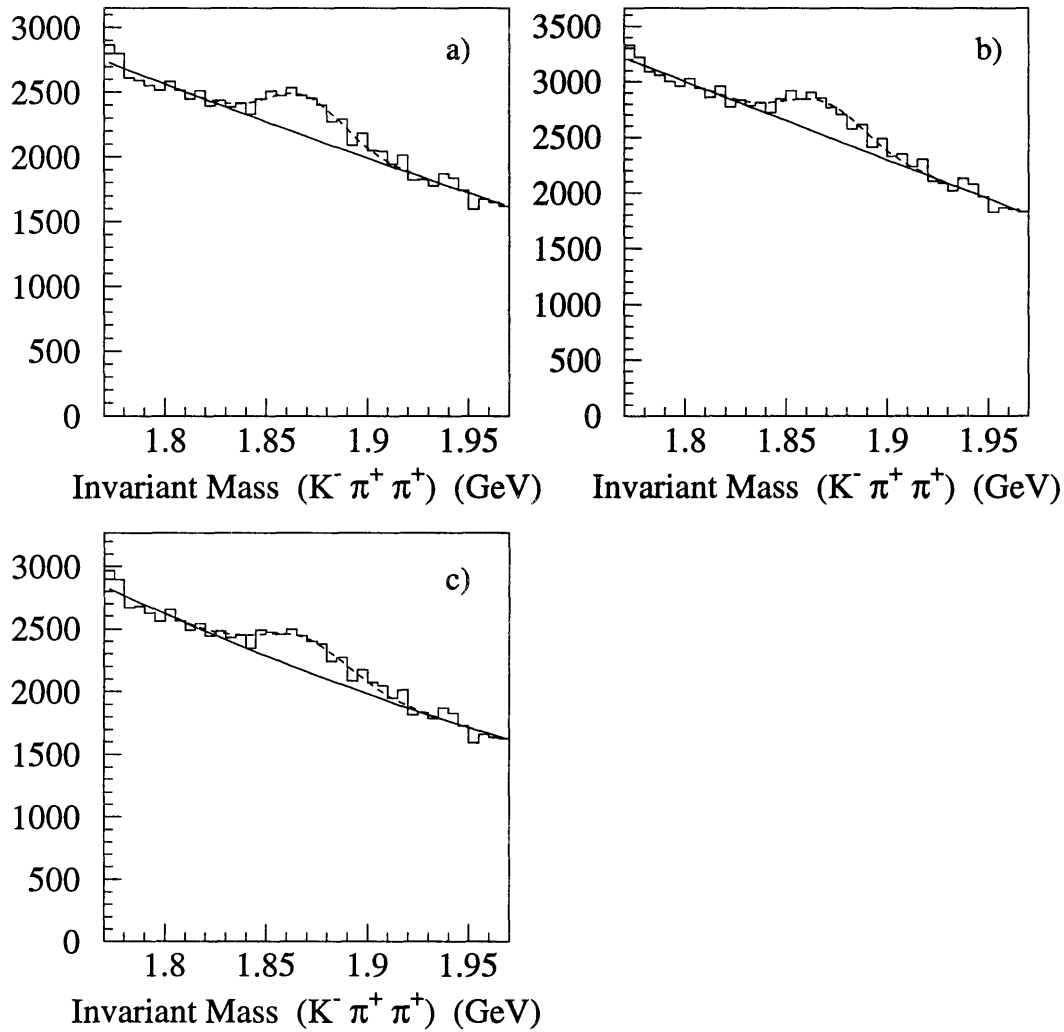


Figure 6.4: Gaussian-plus-polynomial fits to D^+ mass distributions using a) the normalized likelihood scheme, b) the best candidate scheme, and c) no particle identification.

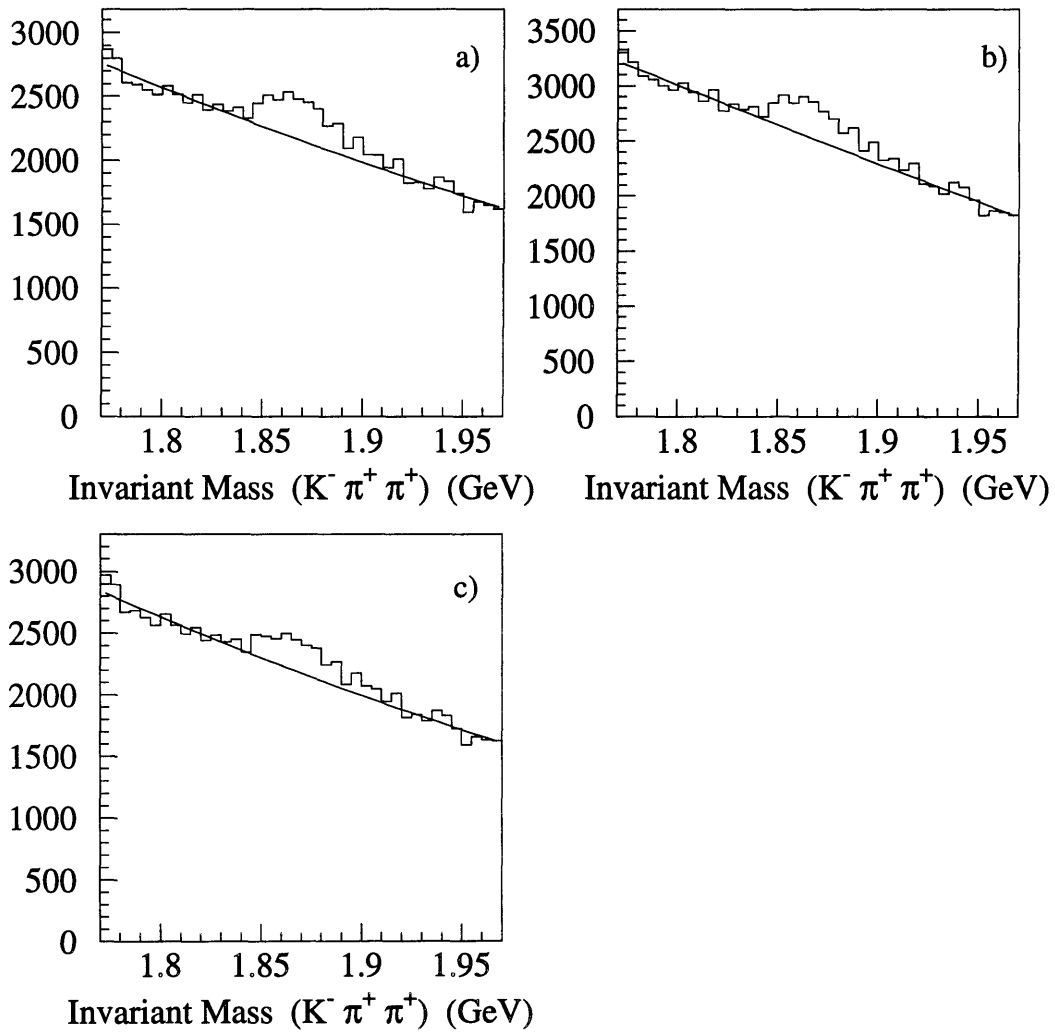


Figure 6.5: Sideband fits to D^+ mass distributions using a) the normalized likelihood scheme, b) the best candidate scheme, and c) no particle identification.

weighted average of the three was taken as the final value of N_{D^+} . The systematic uncertainty in this value was defined by the extrema of the averaged values.

N_{D^+}	Gaussian + Polynomial Fit	Sideband Fit	Combined
Normalized Likelihood	5756 ± 630	5986 ± 829	$5812 \pm 604^{+1003}_{-686}$
Best Candidate	5347 ± 827	5676 ± 694	$5494 \pm 615^{+876}_{-974}$
No Particle ID	6503 ± 743	5729 ± 1016	$6333 \pm 710^{+913}_{-1620}$
Combined			$5847 \pm 368^{+1399}_{-1327}$

Table 6.3: Results of measurements of N_{D^+}

6.4 Extraction of the D^{*+} Branching Fractions

The D^{*+} branching fractions were extracted from N_{D^0} and N_{D^+} as described in section 5.2.1. First, the ratio of the D^+ and D^0 cross sections (R) was calculated according to Eq. 5.5. The systematic uncertainties in N_{D^0} and N_{D^+} were considered to be independent of one another and were added in quadrature. The upper bound uncertainties were combined to obtain the upper bound systematic uncertainty in R :

$$\left(\frac{\delta R^{upper}}{R}\right)^2 = \left(\frac{\delta N_{D^0}^{upper}}{N_{D^0}}\right)^2 + \left(\frac{\delta N_{D^+}^{upper}}{N_{D^+}}\right)^2 + \left(\frac{\delta B(D^0)}{B(D^0)}\right)^2 + \left(\frac{\delta B(D^+)}{B(D^+)}\right)^2 \quad (6.11)$$

and similarly for the lower bound. The relative uncertainties in the D^0 and D^+ branching fractions were significant with respect to the standard deviations of the mean values of N_{D^0} and N_{D^+} , but small compared with the systematic uncertainty in N_{D^+} .

Next, B_{π^+} was derived from R according to Eq. 5.6. The factor r (Eq. 5.4) is a function of the D and D^* masses and of E_{CM} ; the relative uncertainty in r due to these parameters was found to be very small ($(\delta r)/r \sim 0.001$). Dropping terms in δr , the uncertainties in R and B_{π^+} were related by:

$$\frac{\delta B_{\pi^+}}{B_{\pi^+}} = \frac{-r-1}{(1-rR)(1+R)} \cdot R \cdot \frac{\delta R}{R} = -1.41 \cdot \left(\frac{\delta R}{R} \right) \quad (6.12)$$

$B(D^{*+} \rightarrow D^+\pi^0)$ was derived from B_{π^+} according to Eq. 5.1. The uncertainties in the D , D^* , and pion masses had a negligible contribution. The uncertainty in $B(D^{*+} \rightarrow D^+\pi^0)$ was then given by:

$$\delta B(D^{*+} \rightarrow D^+\pi^0) = \frac{1}{2} \cdot \frac{P_{D^+}^3}{P_{D^0}^3} (\delta B_{\pi^+}) = 0.45 \cdot (\delta B_{\pi^+}) \quad (6.13)$$

Finally, $B(D^{*+} \rightarrow D^+\gamma)$ was given by the unitarity constraint:

$$\begin{aligned} B(D^{*+} \rightarrow D^+\gamma) &= 1 - B(D^{*+} \rightarrow D^0\pi^+) - B(D^{*+} \rightarrow D^+\pi^0) \\ &= 1 - B_{\pi^+} \left(1 + \frac{1}{2} \cdot \frac{P_{D^+}^3}{P_{D^0}^3} \right) \end{aligned} \quad (6.14)$$

$$\delta B(D^{*+} \rightarrow D^+\gamma) = - \left(1 + \frac{1}{2} \cdot \frac{P_{D^+}^3}{P_{D^0}^3} \right) (\delta B_{\pi^+}) = -1.45 \cdot (\delta B_{\pi^+}) \quad (6.15)$$

The results are listed in Table 6.4.

Decay Mode	Branching Fraction (%)
$B(D^{*+} \rightarrow D^0\pi^+)$	$64.6 \pm 9.2^{+22.5}_{-23.6}$
$B(D^{*+} \rightarrow D^+\pi^0)$	$29.2 \pm 4.2^{+10.2}_{-10.6}$
$B(D^{*+} \rightarrow D^+\gamma)$	$6.2 \pm 13.4^{+32.7}_{-34.2}$

Table 6.4: Results for the D^{*+} branching fractions.

6.5 Summary

The measured values of the D^{*+} branching fractions are consistent with the current world average. Unfortunately, the statistical and systematic uncertainties are such that the results are consistent with both the recent CLEO II and ARGUS measurements and with the older Mark III measurement (Table 1.2). This measurement does provide an independent con-

sistency check on these values using a completely different measurement technique.

Appendix A

Error Analysis

A.1 General Approach

Consider a set of N observed candidates, consisting of S signal candidates and a background of B candidates, displayed in a histogram with a total of I entries over J bins. Let w_i be a scale factor that maps each entry n_i into a number of candidates, and let b_j be the background level in each bin. Then

$$S = N - B = \sum_i^I w_i n_i - \sum_j^J b_j \quad (\text{A.1})$$

The square of the differential uncertainty in S is then

$$\begin{aligned} (\delta S)^2 &= \left(\sum_i^I w_i \delta n_i \right)^2 + \left(\sum_i^I \delta w_i n_i \right)^2 + \left(\sum_j^J \delta b_j \right)^2 \\ &+ \sum_i^I \delta w_i n_i \sum_k^I w_k \delta n_k - \sum_i^I w_i \delta n_i \sum_j^J \delta b_j - \sum_i^I \delta w_i n_i \sum_j^J \delta b_j \end{aligned} \quad (\text{A.2})$$

The purely statistical uncertainty δn_i is uncorrelated between different entries; the first term therefore can be expressed as

$$\left(\sum_i^I w_i \delta n_i \right)^2 = \sum_i^I w_i \delta n_i \sum_k^I w_k \delta n_k = \sum_i^I w_i^2 (\delta n_i)^2 = \sum_i^I w_i^2 \quad (\text{A.3})$$

The correlation between the number of entries and the background level in each bin is in general weak, since the background for each bin is determined from a fit or other estimate which includes all bins; the same is true of the correlation between the scale factors and the background. There is clearly no correlation between the number of entries and the

scale factor for each entry. Therefore, in averaging the differential uncertainties, the last three cross terms in Eq. A.2 become zero. The RMS uncertainty in the signal size is then a function of three terms:

$$\delta S_{RMS} = \left(\sum_i^I w_i^2 + \left(\sum_i^I \delta w_i n_i \right)^2 + (\delta B)^2 \right)^{1/2} \quad (\text{A.4})$$

1. The sum of the squares of the scale factors. This term represents the purely statistical uncertainty in the number of entries, from which the number of observed candidates is derived.
2. The uncertainty in the scale factor (discussed below).
3. The uncertainty in the background (δB_{RMS}), which may be obtained by various means and may be thought of as a systematic error. However, for a given signal to background ratio, B is directly correlated with N , and $\delta B/B$ in general decreases with N .

A.2 Uncertainties for D Invariant Mass Distribution Fits

A.2.1 Scale Factors

In the D analyses, the scale factor w_i described above corresponds to the product of the joint candidate likelihood (w_D) and the inverse of the joint candidate track efficiency (ϵ_D) (section 6.2.1):

$$w_i = \left(\frac{w_D}{\epsilon_D} \right)_i \quad (\text{A.1})$$

The uncertainty on w_i has two components:

1. A “precision,” or statistical uncertainty. Each w_D is a function of the χ^2 values (Eqs.

6.1 and 6.2) of the candidate's constituent particles. The χ^2 values depend on the measured resolution of each particle identification system (σ_{TOF} , $\sigma_{dE/dx}$). These resolutions are based on very large data samples, and the uncertainties in the resolutions are considered to be relatively small. Similarly, ϵ_D is based on an arbitrarily large Monte Carlo sample and has a negligible statistical error.

2. An ‘‘accuracy,’’ or systematic uncertainty between different particle identification schemes. This term reflects systematic shifts in the particle identification systems or in the Monte Carlo modeling of them. Other Monte Carlo systematics are assumed to be small in comparison. Such shifts will likely have different effects in the different particle identification schemes. Other Monte Carlo systematics are assumed to be small.

The statistical uncertainty is assumed to be negligible compared to the systematic one. The systematic effects are accounted for by comparing the results using the different particle identification schemes. Therefore no term in δw_i appears in δS .

A.2.2 Background Uncertainties

The fitted polynomial background B of a mass distribution fit is given by

$$B = \sum_j b_j = \sum_{j,k} a_k (x_j)^k \quad (\text{A.2})$$

where b_j is the background value in the j th histogram bin, a_k is the k th fit parameter, and x_j is the central mass value of the j th histogram bin. Then

$$(\delta B_{RMS})^2 = \sum_{j,k} \delta a_k (x_j)^k \sum_{m,n} \delta a_n (x_m)^n \quad (\text{A.3})$$

where the $\delta a_k \delta a_n$ are obtained from the fit error matrix.

A.3 Uncertainties in Combined Measurements

Two uncertainties in the weighted average of several individual measurements (e.g., the combination of results from three different particle identification schemes) are quoted:

1. The standard deviation of the mean. For several measurements $A_i \pm \delta A_i$ combined into $\mu \pm \delta\mu$,

$$\delta\mu = \left(\sum_i \frac{1}{(\delta A_i)^2} \right)^{-1/2}. \quad (\text{A.1})$$

2. A systematic uncertainty, in terms of upper and lower bounds defined by the highest and lowest one- σ values of the individual measurements. The uncertainty quoted is the difference between these extrema and the weighted average. For example, if $A + \delta A > B + \delta B$ and $B - \delta B < A - \delta A$, then the average μ of these two measurements and its uncertainty are

$$\mu_{\pm} = \begin{matrix} + (A + \delta A - \mu) \\ - (\mu - (B - \delta B)) \end{matrix}. \quad (\text{A.2})$$

Appendix B

Angular Distributions

B.1 Introduction

The Monte Carlo physics simulations included the charm pair production and D^* decay angular distributions. The angular distributions for $D\bar{D}$ and $D^*\bar{D}^*$ events were obtained following the calculations by Cahn and Kayser [15]. The $D\bar{D}^*$ event distributions were calculated from the $D\bar{D}^*$ production and D^* decay amplitudes; this calculation is described in detail below.

B.2 $D\bar{D}$ and $D^*\bar{D}^*$ Angular Distributions

The $D\bar{D}$ production distribution is straightforward, since the D meson is a pseudoscalar. The angular part of the production amplitude is given by

$$M_{D\bar{D}} \propto \hat{\eta} \cdot \hat{p} \quad (\text{B.1})$$

where $\hat{\eta}$ is the virtual photon polarization vector and \hat{p} is the unit vector in the direction of the D momentum. Squaring the amplitude and summing over the photon polarizations, the angular part of the production cross section is given by

$$\frac{dN_{D\bar{D}}}{d\Omega} \propto 1 - (\hat{n} \cdot \hat{p})^2 = \sin^2\theta \quad (\text{B.2})$$

where \hat{n} is electron beam direction, θ is the angle between the beam direction and the D momentum, and the sum over photon polarizations is given by

$$\sum_{pol} \eta_i \eta_j = \delta_{ij} - \hat{n}_i \hat{n}_j \quad (\text{B.3})$$

The $D^*\bar{D}^*$ distribution is more complicated. The D^* mesons have non-zero spin, and the $D^*\bar{D}^*$ production and D^* decay angular distributions must be expressed together in a joint function. In addition, three different angular momentum states are allowed for the $D^*\bar{D}^*$ system, and the angular distributions are functions of the relative amplitudes of these three states. The resulting distributions are described in Ref. 15.

B.3 $D\bar{D}^*$ Angular Distributions

The $D\bar{D}^*$ production and D^* decay angular distributions are described by joint cross section, one for the $e^+e^- \rightarrow \gamma^* \rightarrow D\bar{D}^* \rightarrow D\bar{D}\pi$ (γ^* = virtual photon) process and one for $e^+e^- \rightarrow \gamma^* \rightarrow D\bar{D}^* \rightarrow D\bar{D}\gamma$ process. Some parameters used in calculating these distributions are defined as follows:

\hat{n} = beam direction

Q = virtual photon 4-momentum

$\hat{\eta}$ = virtual γ polarization

$p = D^*$ 4-momentum, and $\hat{p} = D^*$ direction

$\rho = D^*$ polarization

θ = polar angle between beam direction and D^* direction

$q = \pi$ 4-momentum, and $\hat{q} = \pi$ direction in the D^* rest frame

$k =$ final state γ 4-momentum, and $\hat{k} =$ final state γ direction in the D^* rest frame

$\hat{E} =$ final state γ polarization

$\theta_1 =$ polar angle between D^* direction and π /final state γ direction in the D^* rest frame

$\phi_1 =$ azimuthal angle between D^* direction and π /final state γ direction in the D^* rest frame

$\hat{x}, \hat{y}, \hat{z} =$ lab frame coordinate system, where $\hat{z} = \hat{n}$

$\hat{x}', \hat{y}', \hat{z}' = D^*$ rest frame coordinate system, where:

$$\begin{aligned}\hat{z}' &= \hat{p} \\ \hat{y}' &= (\hat{z}' \hat{\times} \hat{z}) = \frac{\hat{p} \times \hat{n}}{\sin\theta} \\ \hat{x}' &= \hat{y}' \times \hat{z}' = \frac{(\hat{p} \times \hat{n}) \times \hat{p}}{\sin\theta}\end{aligned}$$

The Lorentz-invariant $\bar{D}D^*$ production amplitude (equivalent to the DD^* production amplitude) is

$$M_{D^*D} \propto \varepsilon^{\alpha\beta\mu\nu} Q_\mu \eta_\nu p_\beta \rho_\alpha \quad (\text{B.1})$$

Consider first the $e^+e^- \rightarrow \gamma^* \rightarrow \bar{D}D^* \rightarrow \bar{D}D\pi$ process. The $D^* \rightarrow D\pi$ vertex can be expressed as [15]

$$M_{D\pi} \propto \rho_\sigma (q - r)^\sigma \quad (\text{B.2})$$

where r is the D 4-momentum. The angular distribution is fully described by considering only the pion production cross section; then the total amplitude is

$$M_{\bar{D}D\pi} \propto \varepsilon^{\alpha\beta\mu\nu} Q_\mu \eta_\nu p_\beta \rho_\alpha \rho_\sigma q^\sigma \quad (\text{B.3})$$

Summing over the D^* polarizations,

$$\begin{aligned}M_{\bar{D}D\pi} &\propto \varepsilon^{\alpha\beta\mu\nu} Q_\mu \eta_\nu p_\beta \left(g_{\alpha\sigma} - \frac{p_\alpha p_\sigma}{m_{D^*}^2} \right) q^\sigma \\ &= \varepsilon^{\alpha\beta\mu\nu} Q_\mu \eta_\nu p_\beta q_\alpha - \varepsilon^{\alpha\beta\mu\nu} Q_\mu \eta_\nu p_\beta p_\alpha p_\sigma q^\sigma / m_{D^*}^2\end{aligned} \quad (\text{B.4})$$

where

$$\sum_p \rho_\alpha \rho_\sigma = g_{\alpha\sigma} - \frac{p_\alpha p_\sigma}{m_{D^*}^2} \quad (\text{B.5})$$

his amplitude is Lorentz-invariant, and therefore each term in the expression may be evaluated in any rest frame. Evaluating the second term in the D^* rest frame, it is zero on inspection because the D^* 4-vector p has only one non-zero component. The remaining term can be evaluated in the lab frame. In this frame, the only non-zero term of Q_μ is $Q_4 = E_{CM}$. Then

$$\begin{aligned}
M_{DD\pi} &\propto \varepsilon^{\alpha\beta 4\nu} Q_4 \eta_\nu p_\beta q_\alpha \\
&= E_{CM} \varepsilon^{\nu\alpha\beta} \eta_\nu p_\beta q_\alpha \\
&= (E_{CM}) (\vec{p} \times \vec{\eta}) \cdot \vec{q}
\end{aligned} \tag{B.6}$$

Squaring this amplitude and summing over virtual photon polarizations,

$$\begin{aligned}
\sum_{\eta} |M_{DD\pi}|^2 &\propto \sum_{\eta} |\vec{q} \cdot (\vec{p} \times \vec{\eta})|^2 \\
&= \sum_{\eta} \varepsilon^{ijk} \eta_i q_j p_k \varepsilon^{rst} \eta_r q_s p_t \\
&= \varepsilon^{ijk} q_j p_k \varepsilon^{ist} q_s p_t - \varepsilon^{ijk} q_j p_k \varepsilon^{rst} q_s p_t n_i n_r \\
&\quad \text{(where } \sum_{\eta} \eta_i \eta_r = \delta_{ir} - n_i n_r) \\
&\propto (\hat{q} \times \hat{p}) \cdot (\hat{q} \times \hat{p}) - (\hat{q} \cdot (\hat{p} \times \hat{n}))^2 \\
&= \sin^2 \theta - (\sin \theta_1 \sin \phi_1 \sin \theta)^2 \propto \frac{dN_{DD\pi}}{d\Omega}
\end{aligned} \tag{B.7}$$

Next consider the $e^+ e^- \rightarrow \gamma^* \rightarrow \bar{D} D^* \rightarrow \bar{D} D \gamma$ process. The $D^* \rightarrow D \gamma$ vertex has the same structure as the $\bar{D} D^*$ production vertex:

$$M_{D\gamma} \propto \varepsilon^{abcd} k_c E_d p_b \rho_a \tag{B.8}$$

The total amplitude is

$$M_{DD\gamma} \propto \varepsilon^{\alpha\beta\mu\nu} Q_\mu \eta_\nu p_\beta \rho_\alpha \varepsilon^{abcd} k_c E_d p_b \rho_a$$

Summing over D^* polarizations,

$$M_{DD\gamma} \propto \varepsilon^{\alpha\beta\mu\nu} Q_\mu \eta_\nu p_\beta \varepsilon^{abcd} k_c E_d p_b - \varepsilon^{\alpha\beta\mu\nu} Q_\mu \eta_\nu p_\beta \varepsilon^{abcd} k_c E_d p_b \rho_\alpha \rho_a / m_{D^*} \quad (\text{B.9})$$

Evaluating the second term in the D^* rest frame, it is zero on inspection because the D^* 4-vector p has only one non-zero component. Evaluating the first part of the remaining term in the lab frame and the second part in the D^* rest frame,

$$\begin{aligned} M_{DD\gamma} &\propto \left(\varepsilon^{\alpha\beta 4\nu} Q_4 \eta_\nu p_\beta \right) \left(\varepsilon^{\alpha 4 cd} k_c E_d p_4 \right) \\ &= (E_{CM}) (m_{D^*}) (\vec{p} \times \vec{\eta}) \cdot (\vec{k} \times \vec{E}) \end{aligned} \quad (\text{B.10})$$

Squaring this amplitude and summing over virtual photon and final state photon polarizations,

$$\begin{aligned} \sum_{\eta, E} |M_{DD\gamma}|^2 &\propto \sum_{\eta, E} \varepsilon^{ijk} p_j \eta_k \varepsilon^{imn} k_m E_n \varepsilon^{rst} p_s \eta_t \varepsilon^{ruv} k_u E_v \\ &= \varepsilon^{ijk} p_j \varepsilon^{imn} k_m \varepsilon^{rst} p_s \varepsilon^{ruv} k_u (\delta_{kt} - n_k n_t) (\delta_{nv} - k_n k_v) \\ &\quad (\text{where } \sum_E E_n E_v = \delta_{nv} - k_n k_v) \\ &\propto 1 - (\hat{n} \cdot \hat{k})^2 + 2(\hat{p} \cdot \hat{k})(\hat{n} \cdot \hat{p})(\hat{n} \cdot \hat{k}) \\ &= 1 + (\cos\theta \cos\theta_1)^2 - (\sin\theta \sin\theta_1 \cos\phi_1)^2 = \frac{dN_{DD\gamma}}{d\Omega} \end{aligned} \quad (\text{B.11})$$

References

1. Particle Data Group, L. Montanet *et al.*, Review of Particle Properties, *Phys. Rev.* **D50** (1994) 1173.
2. Mark III Collaboration, J. Adler *et al.*, *Phys. Lett.* **B208** (1988) 152.
3. CLEO Collaboration, F. Butler *et al.*, *Phys. Rev. Lett.* **69** (1992) 2041.
4. ARGUS Collaboration, H. Albrecht *et al.*, Preprint DESY 94-111, July 1994.
5. Particle Data Group, K. Hikasa *et al.*, Review of Particle Properties, *Phys. Rev.* **D45** (1992) S1.
6. J. L. Rosner, in Particles and Fields 3, *Proceedings of the Banff Summer Institute, Banff Canada 1988*, A. N. Kamal and F. C. Khanna, eds., World Scientific, Singapore (1989), 395.
7. J. F. Amundson, *et al.*, *Phys. Lett.* **B296** (1992) 415.
8. G. A. Miller and P. Singer, *Phys. Rev.* **D37** (1988) 2564.
9. L. Angelos, and G. P. Lepage, *Phys. Rev.* **D45** (1992) R3021.
10. M. H. Ye, and Z. P. Zheng, *Proceedings of the 1989 International Symposium on Lepton and Photon Interactions at High Energies*, Stanford University, Stanford (1989) 122.
11. D. H. Perkins, *Introduction to High Energy Physics*, 3rd ed., Addison-Wesley Publishing Company, Inc. (Menlo Park), (1987) 38-40.
12. E. Eichten *et al.*, *Phys. Rev.* **D21**, (1980) 203.
13. W. S. Lockman, Mark III memorandum, “ D and D_s Production in the Range $3.8 < \sqrt{s} < 4.5$ GeV”, March 30, 1987.
14. M. W. Coles *et al.*, *Phys. Rev.* **D26** (1982) 2190.
15. R. N. Cahn and B. Kayser, *Phys. Rev.* **D22** (1980) 2752.

Vita

Oliver Bardon was born September 17, 1966 in New York City, New York, to Marcel Bardon and Renate M. Bardon. He graduated from Langley High School in McLean, Virginia, in the Spring of 1984 and entered the University of Virginia in the following Fall. He received the degree of Bachelor of Arts with a major in Physics from the University of Virginia in the Spring of 1988. In the Fall of 1988, he enrolled in the Massachusetts Institute of Technology as a graduate student in the department of physics. While an MIT student, he worked at the Stanford Linear Accelerator Center (SLAC) as a member of both the Beijing Spectrometer (BES) collaboration and the SLC Large Detector (SLD) collaboration. In 1994 he married Christiana Goh of Claremont, California.